Quantifying Marine Carbon Dioxide Removal via Alkalinity Enhancement Across Circulation Regimes Using ECCO-Darwin and 1D Models

Kay Suselj[1], Dustin Carroll[2,1], Daniel Whitt[3], Bridget Samuels[4], Dimitris Menemenlis[2], Hong Zhang[1], Nate Beatty[5], Anna Savage[5]

[1]Jet Propulsion Laboratory, California Institute of Technology, Pasadena, CA, USA
[2]Moss Landing Marine Laboratories, San José State University, Moss Landing, CA, USA
[3]NASA Ames Research Center, Moffett Field, CA, USA
[4]Clima-Tek Analytics LLC, Pasadena, CA
[5]Running Tide, Inc., Portland, ME, USA

Key Points:

- Regional open-ocean alkalinity enhancement (OAE) is simulated in five archetypal ocean regimes using the data-assimilative ECCO-Darwin model.
- Ocean dynamics drive substantial regional differences in OAE efficiency.
- A 1D model is introduced to isolate and quantify OAE efficiency sensitivity to vertical transport processes.

Corresponding author: Kay Suselj, `kay.suselj@jpl.nasa.gov`

Abstract

Ocean Alkalinity Enhancement (OAE) is emerging as a viable method for removing anthropogenic CO_2 emissions from the atmosphere to mitigate climate change. To achieve substantial carbon reductions, OAE would need to be deployed at scale across the global ocean. Hence, there is a need to quantify how the efficiency of OAE varies globally across a range of space-time scales in preparation for field deployments. Here we develop a marine carbon dioxide removal (mCDR) efficiency evaluation framework based on the data-assimilative ECCO-Darwin ocean biogeochemistry model, which separates and quantifies two key factors over seasonal to multi-annual timescales: 1) mCDR potential, which quantifies the ability of seawater to store additional carbon after an alkalinity perturbation; and 2) dynamical mCDR efficiency, representing the impact of ocean advection, mixing, and air-sea CO_2 exchange. We apply this framework to virtual OAE deployments in five archetypal ocean circulation regimes with different mCDR potentials and dynamical efficiencies. The simulations highlight the importance of the dynamical factors, especially vertical transport, in driving differences in efficiency. To rapidly isolate and quantify the factors that determine dynamical efficiency, we develop a reduced complexity 1D model, rapid-mCDR. We show that combining the rapid-mCDR model with existing ECCO-Darwin output allows for rapid characterization of OAE efficiency at any location globally. Thus, these tools can be readily employed by research teams and industry to model future field deployments and contribute to essential Monitoring, Reporting, and Verification (MRV) efforts.

Plain Language Summary

In an effort to counteract ongoing climate warming, engineering methods have been proposed to artificially enhance marine carbon dioxide removal (mCDR) from the atmosphere by reducing the ocean's acidity or enhancing its alkalinity — this is called Ocean Alkalinity Enhancement (OAE). However, implementing OAE at a scale where it would have a significant impact on the anthropogenic perturbation to atmospheric carbon dioxide is costly and challenging, and many uncertainties remain regarding how effective OAE would be. This paper addresses the practical question of where and when might OAE be most effective, with a specific focus on exposing how regional variations in ocean circulation might lead to differences in the effectiveness of OAE. Several virtual scaled-up regional and multi-decadal OAE deployments are simulated in five different open-ocean circulation regimes in a state-of-the-art, global model of ocean circulation and biogeochemistry. The results show that different ocean circulation regimes yield significant differences in the effectiveness of OAE. These results help scientists and other stakeholders understand and quantify the range of possible impacts of circulation variability on OAE efficiency.

1 Introduction

The major aim of the Paris Agreement is to reduce emissions and enhance carbon sinks to keep the global temperature increase well below 2 degrees in this century (Rogelj et al., 2018; Schimel & Carroll, 2024). This limit requires a 50% reduction in anthropogenic carbon dioxide (CO_2) emissions by 2030, with net emissions nearly eliminated by 2050. This effort will require almost complete decarbonization of the world's energy supply (Friedlingstein et al., 2022; Palter et al., 2023). Furthermore, the IPCC's 6th assessment report has emphasized that atmospheric CO_2 removal on the gigaton scale will be necessary to reach net zero emissions (IPCC, 2022).

Due to the vast carbon reservoir (i.e. the mass of carbon) in the global oceans, which is already a sink for roughly one quarter of anthropogenic CO_2 emissions (Gruber et al., 2019; Friedlingstein et al., 2022), various methods for marine carbon dioxide removal (mCDR) have been proposed to accelerate the net transfer of carbon from the atmosphere to the ocean (National Academies of Sciences, Engineering, and Medicine, 2022). Ocean Alkalinity Enhancement (OAE; Renforth & Henderson, 2017) is one such method proposed to bolster the uptake of atmospheric CO_2 by the ocean. Examples of particular OAE approaches include: 1) reduction of seawater acidity through electrochemical processes (House et al., 2007), 2) deployment of alkaline substances on the surface ocean, and 3) enhanced weathering of alkaline minerals on land that accelerates their transfer to the coastal ocean (Taylor et al., 2016; Montserrat et al., 2017). See Eisaman et al. (2023) for a detailed technical review of various OAE approaches. Overall, National Academies of Sciences, Engineering, and Medicine (2022) have rated OAE efficacy as "high confidence" with durability and scalability as "medium-high", yet the knowledge base remains "low-to-medium". Thus, additional research to advance the knowledge base for OAE is a priority.

The core principle of OAE leverages tight coupling between ocean alkalinity (*Alk*) and the nonlinear marine carbonate chemistry system (Middelburg et al., 2020). OAE is generally focused on the deployment of *Alk* at, or near the ocean surface, which transforms aqueous carbon dioxide (CO_2) into bicarbonate (HCO_3^-) and carbonate ions (CO_3^{2-}) through a series of rapid acid-base reactions (Zeebe & Wolf-Gladrow, 2001). This chemical adjustment leads to a reduction in aqueous carbon dioxide (CO_2^{aq}) concentrations and thus lowers the partial pressure of carbon dioxide in seawater ($p\mathrm{CO}_2^{aq}$). If the *Alk* addition and $p\mathrm{CO}_2^{aq}$ reduction occur in the surface ocean, it can drive ocean uptake of CO_2 from the atmosphere or decrease the rate of CO_2 outgassing, both of which result in a net increase in ocean carbon uptake. If the net CO_2 absorbed from the atmosphere remains in the surface ocean, it tends to restore surface-ocean $p\mathrm{CO}_2^{aq}$ and therefore the ocean-atmosphere $p\mathrm{CO}_2$ gradient back toward the values it would have in the absence of OAE deployment. The efficiency of OAE, which is typically defined by the ratio of moles of CO_2 removed from the atmosphere per mole of deployed alkalinity, however, remains poorly constrained.

For typical surface-ocean carbon chemistry, OAE has the potential to remove roughly 0.8 moles of CO_2 from the atmosphere per mole of deployed *Alk* (Renforth & Henderson, 2017; Tyka et al., 2022). The actual amount of atmospheric CO_2 removed, however, hinges on the complex interplay of ocean physics and biogeochemistry, and thus can deviate from this value. While ocean carbonate chemistry reactions occur nearly instantaneously and CO_2 in the atmosphere mixes efficiently on the timescale of days, the adjustment of ocean $p\mathrm{CO}_2^{aq}$ perturbations to pre-deployment levels via air-sea CO_2 flux occurs over weeks to years (Jones et al., 2014; He & Tyka, 2023). This adjustment process takes place against the backdrop of multi-scale ocean dynamics, with timescales ranging from seconds to thousands of years (Williams & Follows, 2011). Ocean dynamics strongly influence the marine carbonate system state and can sequester OAE-perturbed waters to depth far away from the air-sea interface, thereby reducing or delaying the removal of atmospheric CO_2 and the efficiency of OAE. Furthermore, the total reduction of atmospheric CO_2 can be smaller than the mCDR-driven sequestration, due to carbon cycle feedbacks with other components of the Earth System (see e.g., Tyka, 2024).

Several prior investigations have used numerical ocean models to show that the efficiency of OAE is subject to considerable regional and temporal variability across the global ocean and specifically that the ocean circulation significantly impacts OAE efficiency (Ilyina et al., 2013; González et al., 2018; Burt et al., 2021; He & Tyka, 2023; Yamamoto et al., 2024). Most recently, Zhou et al. (2025) used a global ocean and sea-ice model (Community Earth System Model version 2; CESM2), forced by atmospheric reanalysis, to quantify how ocean dynamics shape OAE efficiency globally. However, their analysis was limited to pulse OAE experiments conducted for the year 1999, using a single model unconstrained by the ocean observations. Notably, CESM is known to exhibit several biases, particularly in mixed layer depth — a factor that directly affects the response timescale to an OAE perturbation (Griffies et al., 2009; Danabasoglu et al., 2014; Jones et al., 2014). As a result, some of their findings may not be fully representative of real-world behavior. Consequently, key questions remain unresolved. For example: (1) How does OAE efficiency vary across archetypal regional-scale circulation regimes? and (2) How do spatial variations in efficiency evolve temporally under the influence of the seasonal cycle and interannual climate variability? Fully addressing these high-priority questions requires multi-model studies, and especially the use of data-constrained models simulating a wide range of OAE scenarios.

In this study, we take a necessary step forward in building the knowledgebase needed to answer these open questions by simulating regional-scale open-ocean OAE deployments of monthly-to-multi-decadal duration in a data-constrained global model of ocean circulation, sea ice, and biogeochemistry/ecosystem dynamics, ECCO-Darwin (Carroll et al., 2020, 2022, 2024). The data constraints significantly reduce ocean physical biases that are common in unconstrained ocean models. For example, the representation of ocean mixed layer depth in data constrained ECCO-Darwin model (Forget, Fukumori, et al., 2015; Forget, Campin, et al., 2015; ECCO Consortium et al., 2021) generally shows significantly better agreement with observations compared to unconstrained models (e.g. Griffies et al., 2009; Tsujino et al., 2020; Treguier et al., 2023). We focus on regional and multi-decadal scale deployments based on the hypothesis that they might achieve a "goldilocks" trade-off: sufficiently small to be plausibly achievable yet sufficiently large to meaningfully reduce global warming in the 21st century. We also consider continuous virtual OAE simulations as a practical complement to monthly "pulse" OAE simulations, since continuous experiments better characterize the typical efficiency of OAE as it varies substantially with time, either seasonally or interannually. We elucidate the impact of ocean dynamics on OAE efficiency by separating and comparing 1) the OAE potential, which is calculated by assuming that the *Alk* perturbations remain in the surface layer of a hypothetical static ocean and that air-sea exchange fully and instantly restores $p\mathrm{CO}_2^{aq}$ to pre-deployment levels; and 2) the dynamic efficiency of OAE, which is computed by differencing the simulated ocean CO_2 flux from a counterfactual baseline simulation without OAE but having an otherwise identical dynamical ocean, normalized by OAE potential. Unlike previous studies (e.g. He & Tyka, 2023; Tyka, 2024), which combine both OAE dynamical efficiency and potential into a single metric, we separate and individually quantify the impact of these two key components in our analysis. We note there is precedent for this separation of terms (Wang et al., 2023), with previous studies also making a distinction between the maximum expected impact and the transient approach to that impact (Yamamoto et al., 2024). We note that Yamamoto et al. (2024) take a different approach to their computation by normalizing relative to direct air capture and their efficiency term is dynamic, while the mCDR potential term is more implicit.

Although the efficiency of OAE is nominally different across space-time domains, we build new understanding by presenting a series of five key case studies of OAE deployments at different locations, representative of distinct open-ocean circulation archetypes. The regimes include a quiescent subtropical gyre contrasted with four energetic regimes, including one in each of the following: a mid-latitude western boundary current, the Antarctic Circumpolar Current, a low-latitude equatorial upwelling region, and a high-latitude deep-water formation region. Our results support the hypothesis that vertical transport processes have an outsized impact on OAE efficiency. Hence, we isolate and more fully quantify the sensitivity of OAE efficiency to vertical transport processes by developing and analyzing a 1D vertical ocean biogeochemical model, called *rapid-mCDR*.

2 Methods

This section defines the metrics used to quantify mCDR efficiency by OAE (Section 2.1), describes the virtual OAE deployments and related numerical experiments (Section 2.2), reviews the ECCO-Darwin state estimate framework (Section 2.3), and presents the new 1D rapid-mCDR model for simulation of OAE-attribued Dissolved Inorganic Carbon (DIC) and Alk cycling and mCDR efficiency (Section 2.4).

2.1 Metrics for Quantifying OAE-driven Atmospheric CO_2 Removal

Net CO_2 removal from the atmosphere to the oceans ΔDIC_{tot} (in mol C) is evaluated by integrating the difference in CO_2 flux (Δf_C in mol C m^{-2} s^{-1}) between OAE-perturbed simulations (with alkalinity perturbation ΔAlk_{tot} in mol Alk) and the baseline simulation, integrated over a discrete time interval t after deployment:

$$\Delta DIC_{tot}(t) = \int_{t_s}^{t_s+t} \int_A \Delta f_C \ \mathrm{d}A \ \mathrm{d}t, \tag{1}$$

with t_s marking the start of OAE deployment and A the global ocean surface area. Hence, Eq. 1 is equivalent to the volume integral of the OAE-perturbation to the local concentrations $\int_V \Delta DIC(t)dV$ over the ocean volume V where ΔDIC is the perturbation from the baseline DIC concentration (in mol C m^{-3}). Throughout the paper, the subscript tot on DIC and Alk denotes total mass in the ocean (units of moles) in contrast to concentrations (units of mol m^{-3}) in the absence of subscript tot.

In the numerical experiments presented here, the atmosphere is approximated as an infinite, imperturbable reservoir of CO_2 and the atmospheric and ocean physical states are unperturbed by OAE; the OAE-perturbation therefore acts to decrease $p\mathrm{CO}_2^{aq}$. Other net ocean carbon chemistry responses to OAE are quantified similarly as differences between the OAE-perturbed and baseline simulations.

As in previous work (He & Tyka, 2023; Zhou et al., 2025), we define the practical measure of mCDR efficiency (η) as the ratio between the cumulative number of moles DIC absorbed by the ocean and cumulative number of moles Alk that were added to the surface ocean:

$$\eta(t) = \frac{\Delta DIC_{tot}(t)}{\Delta Alk_{tot}(t)}, \tag{2}$$

where the time-dependent $\Delta DIC_{tot}(t)$ is calculated from simulation output using Eq. 1 and time-dependent $\Delta Alk_{tot}(t)$ is calculated from simulation forcing, which can be expressed as a surface-ocean alkalinity flux perturbation per unit time and deployment area (A_d) associated with the OAE introduced Alk Δf_A:

$$\Delta Alk_{tot}(t) = \int_{t_s}^{t_s+t} \int_{A_d} \Delta f_A \ \mathrm{d}A \ \mathrm{d}t. \tag{3}$$

Again, Eq. 3 is equivalent to the volume integral of the OAE-perturbation in the local concentrations $\int_V \Delta Alk(t)dV$ over the ocean volume V. We note that if a given alkalinity perturbation ΔAlk_{tot} is added instantaneously and uniformly to a surface-ocean area A_d at a time t_s, $\Delta f_A = \delta(t-t_s)\Delta Alk_{tot}/A_d$, where $\delta(t)$ is the Dirac delta function. We note that our definition of efficiency $\eta(t)$ in Eq. 2 and in He and Tyka (2023) are equivalent. Throughout the paper, a variety of metrics like η will be used that formally have units of moles DIC per mole Alk, and this mole per mole unit will be implied but not stated explicitly.

To provide insight into the mechanisms regulating η, we next characterize and separate the contributions of the OAE perturbation ΔAlk_{tot} and the mCDR response ΔDIC_{tot} to $\Delta p\mathrm{CO}_2^{aq}$, following Takahashi et al. (1993):

$$\Delta p\mathrm{CO}_2^{aq} \approx \frac{\partial p\mathrm{CO}_2^{aq}}{\partial DIC}\frac{\Delta DIC_{tot}}{V} + \frac{\partial p\mathrm{CO}_2^{aq}}{\partial Alk}\frac{\Delta Alk_{tot}}{V}. \tag{4}$$

To ensure the accuracy of this expression, the perturbations ΔDIC_{tot} and ΔAlk_{tot} should be small and evenly distributed over a volume V with approximately constant sensitivities $\partial p\mathrm{CO}_2^{aq}/\partial DIC$ and $\partial p\mathrm{CO}_2^{aq}/\partial Alk$. Other factors that are typically important drivers of variability in $p\mathrm{CO}_2^{aq}$, such as temperature and salinity, are identical in the OAE-perturbed and baseline simulations and thus do not appear in Eq. 4.

A useful relationship, which we call mCDR potential, can be defined as a ratio of net CO_2 uptake ($\Delta DIC_{tot,pot}$) and the amount of alkalinity added (ΔAlk_{tot}) to seawater, assuming complete air-sea equilibration of the alkalinity perturbation by substituting $\Delta p\mathrm{CO}_2^{aq} = 0$ into Eq. 4 and rearranging:

$$mCDR_{pot} \equiv \frac{\Delta DIC_{tot,pot}}{\Delta Alk_{tot}} = -\frac{\partial p\mathrm{CO}_2^{aq}}{\partial Alk}\left(\frac{\partial p\mathrm{CO}_2^{aq}}{\partial DIC}\right)^{-1} = -\frac{DIC}{Alk}\frac{\gamma_{Alk}}{\gamma_{DIC}}, \tag{5}$$

where $\Delta DIC_{tot,pot}$ is defined to be the ΔDIC_{tot} required to adjust $p\mathrm{CO}_2^{aq}$ to the baseline state; i.e., $\Delta p\mathrm{CO}_2^{aq} = 0$. The $p\mathrm{CO}_2^{aq}$ sensitivities to DIC and Alk are $\gamma_{DIC} = \frac{DIC}{p\mathrm{CO}_2^{aq}}\frac{\partial p\mathrm{CO}_2^{aq}}{\partial DIC}$ and $\gamma_{Alk} = \frac{Alk}{p\mathrm{CO}_2^{aq}}\frac{\partial p\mathrm{CO}_2^{aq}}{\partial Alk}$ (e.g. Sarmiento & Gruber, 2006, page 329), and γ_{DIC} is the familiar buffer or Revelle factor (Takahashi et al., 1980). Typical latitude dependencies or maps of DIC, Alk, γ_{DIC}, and γ_{Alk} can be readily found in textbooks and published literature, for example in Takahashi et al. (1993) or Chapter 8 of Sarmiento and Gruber (2006).

We note that our definition of mCDR potential differs from that of Wang et al. (2023), who use CDR potential to refer to the total DIC uptake for a given alkalinity injection, i.e., $\Delta DIC_{tot,pot}$ in our terminology. Our definition, in which the potential represents the DIC uptake per unit Alk injected, highlights the intrinsic dependence of the potential on the unperturbed ocean baseline state and facilitates easier comparisons between experiments with different magnitudes of injected alkalinity.

Since the $mCDR_{pot}$ defined by Eq. 5 varies across time and space, it is necessary to average values to obtain a single representative numeric estimate of $mCDR_{pot}$. The potential carbon removal $\Delta DIC_{tot,pot}$ for a given OAE experiment can be then expressed as:

$$\Delta DIC_{tot,pot}(t) \approx \langle mCDR_{pot} \rangle \Delta Alk_{tot}(t), \tag{6}$$

where the brackets around $\langle mCDR_{pot} \rangle$ indicate a space-time average of surface-ocean $mCDR_{pot}$ in the baseline simulation where and when the alkalinity is deployed. We quantify $mCDR_{pot}$ in Eq. 5 offline using Python toolbox for solving the marine carbonate system (*PyCO2SYS*; Humphreys et al., 2022) and the relevant gridded output from the baseline ECCO-Darwin simulation, as well as with the OceanSODA-ETHZ dataset (Gregor & Gruber, 2021) for comparison (see Supporting Information Text S2).

Hypothetically, $mCDR_{pot} = \eta$ and $\Delta DIC_{tot,pot} = \Delta DIC_{tot}$ if 1) all ΔAlk remains in the surface-ocean layer at the location where it is injected and 2) the air-sea CO_2 flux perturbation Δf_C transfers exactly the atmospheric CO_2 needed to restore the OAE-perturbated $\Delta p CO_2^{aq}$ to zero. However, it will be shown that the efficiency of OAE η is typically (but not always) substantially less than $mCDR_{pot}$, even over decadal timescales. This is primarily because OAE-perturbed waters can be isolated from atmospheric exchange for up to thousands of years (England, 1995) via downward ocean transport and mixing driven by circulation dynamics. Hence, we define the *dynamical mCDR efficiency* as:

$$mCDR_{eff}(t) = \frac{\eta(t)}{\langle mCDR_{pot} \rangle}. \tag{7}$$

Eq. 7 separates η into a product of potential ($mCDR_{pot}$) and dynamical-efficiency ($mCDR_{eff}$) components, which provides a meaningful separation into drivers relating to carbon chemistry and ocean dynamics, respectively. The time dependence of $mCDR_{eff}$ or η is governed by the type of OAE deployment, particularly by the temporal evolution of the deployed alkalinity.

In order to evaluate the significance of vertical transport of OAE-modified waters and specifically the extent to which their mCDR potential has been realized as a function of space and time, we define $mCDR_{equil}$, following Wang et al. (2023). $mCDR_{equil}$ is a space-time resolved version of $mCDR_{eff}$, where ΔDIC_{tot} and ΔAlk_{tot} are replaced with local ΔDIC and ΔAlk concentrations:

$$mCDR_{equil} = \frac{1}{\langle mCDR_{pot} \rangle} \frac{\Delta DIC}{\Delta Alk}. \tag{8}$$

$mCDR_{equil}$ values of one indicate that the mCDR has been fully realized relative to the potential where the alkalinity was deployed, while values closer to zero suggest that only a small fraction of that potential has been achieved. To better understand the vertical extent of OAE-modified waters, we will show the vertical distribution of horizontally-averaged $mCDR_{equil}$ values for select deployments. All points where $\Delta Alk = 0$ are omitted from the calculation.

Finally, in order to better characterize overall mCDR efficiency of deployment location and seasonality/interannual variability of net CO_2 uptake for continuous OAE experiments with a time-constant Alk flux f_A over many years, we define $mCDR^{p}_{eff}$:

$$mCDR^{p}_{eff}(t) = \frac{1}{\langle mCDR_{pot} \rangle} \frac{\partial/\partial t\ \Delta DIC_{tot}}{\partial/\partial t\ \Delta Alk_{tot}} = \frac{1}{\langle mCDR_{pot} \rangle} \frac{\int_A \Delta f_C(t)\,\mathrm{d}A}{A_d\ \Delta f_A}, \tag{9}$$

which is the ratio of the OAE-perturbed CO_2 flux to the Alk flux at a given time normalized by $mCDR_{pot}$ (rather than integrating the fluxes in time since the beginning of the experiment as in $mCDR_{eff}$ and η). Thus, $mCDR^{p}_{eff}(t)$ is a rate-based measure of efficiency at a given time, whereas $\eta(t)$ and $mCDR_{eff}(t)$ are cumulative ocean reservoir-based measures of efficiency at a given time. The superscript ‘p’ stands for “pulse” for reasons described below in Section 2.2.5.

Symbol/Term	Brief Explanation	Section Guide
$mCDR_{pot}$	mCDR potential, net CO_2 uptake per unit of deployed alkalinity assuming instantaneous and complete adjustment of ocean $p\mathrm{CO}_2^{aq}$ with respect to the unperturbed baseline situation via air-sea CO_2 flux	Section 2.1
η	A cumulative measure of net CO_2 uptake efficiency per unit of deployed alkalinity based on the OAE-perturbed ocean reservoirs of alkalinity and carbon	Section 2.1
$mCDR_{eff}$	A cumulative measure of the dynamical efficiency of OAE relative to its potential	Section 2.1
$mCDR_{equil}$	A local, space-time resolved measure of the dynamical efficiency of OAE relative to its potential at the deployment location	Section 2.1
$mCDR^{p}_{eff}$	A rate-based measure of the efficiency of OAE computed from the continuous OAE experiments, but designed to represent the efficiency of pulse experiments.	Section 2.2.5
Baseline Simulation	Unperturbed ECCO-Darwin state estimate, representing real-world ocean conditions	Section 2.3
Continuous Experiment	Persistent, steady OAE injection flux over multiple years	Section 2.2.3
Pulse Experiment	A transient or instantaneous OAE injection flux	Section 2.2.4
rapid-mCDR(DeployAve)	Reduced-complexity rapid-mCDR model results neglecting horizontal transport	Section 2.4
rapid-mCDR(TransAve)	Rapid-mCDR model results accounting for horizontal transport	Section 2.4

Table 1. List of key terms/quantities and the associated sections in this paper.

2.2 Virtual OAE deployments

In this section, we describe our numerical experiments, including the baseline simulation and a suite of regional continuous and pulse OAE deployment scenarios that provide the basis for estimating the metrics described in Sec. 2.1 and answering the questions posed in the Introduction.

2.2.1 Baseline simulation

The impacts and net CO_2 uptake attributed to OAE are evaluated with respect to the baseline simulation. This *baseline* simulation of the full time-evolving global physical and biogeochemical state, including the air-sea CO_2 flux and surface-ocean carbonate state necessary for calculating the metrics in Sec. 2.1, represents the natural ocean state in the absence of any OAE perturbations from January 1, 1995 to December 31, 2017. The simulation is similar to several previous runs of ECCO-Darwin, which generally agree well with in-situ observations over the global ocean and in various OAE deployment sites (see Supporting Information Text S1 and Figs. S1–S2). The methods underpinning ECCO-Darwin are briefly summarized in Sec. 2.3.

2.2.2 OAE deployment sites

Five deployment regions were chosen to be representative of diverse dynamical and biogeochemical open-ocean conditions that serve as archetypes to help us build understanding of how various ocean circulation regimes impact OAE efficiency. Figure 1 and Table 2 describe the chosen OAE deployment sites. The Supporting Information Figs. S3 and S2 illustrate the surface ocean context of the five regions and demonstrate that ECCO-Darwin provides a realistic representation of surface ocean conditions.

The following five mCDR experiments are considered:

- The *North Atlantic Subduction (NAS)* experiment represents unique conditions found in subpolar regions associated with subduction driven by heat loss, sea-ice formation and brine rejection, strong seasonally-driven vertical mixing, and seasonal biological CO_2 uptake.

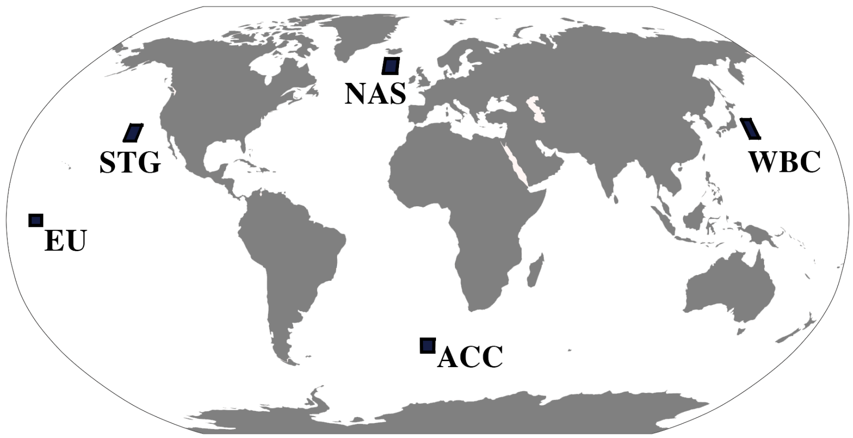

Figure 1. OAE deployment sites considered in this study.

- The *Western Boundary Current (WBC)* experiment is representative of mid-latitude conditions with strong horizontal currents and shear, along with intense vertical mixing.
- The *Antarctic Circumpolar Current (ACC)* experiment represents conditions found in the Southern Ocean, which are associated with strong zonal currents, seasonal sea-ice cover, large-scale upwelling fronts, and seasonal biological uptake.
- The *Equatorial Upwelling (EU)* experiment is centered over the narrow upwelling zone of the Tropical Pacific Ocean and is characterized by strong CO_2 outgassing and biological uptake; its interannual variability tends to be dominated by El Niño–Southern Oscillation events (ENSO), which are significant relative to the seasonal cycle.
- The *Subtropical Gyre (STG)* experiment is centered over a region dominated by relatively slow surface-ocean currents and weaker primary production. It is positioned near the eastern margin of the North Pacific Subtropical Gyre, mainly because site selection closer to land should enhance deployment feasibility.

2.2.3 Continuous OAE deployments

Alkalinity is released at each site using continuous and pulse release protocols. For *continuous OAE experiments*, a constant *Alk* flux f_A is applied to the ECCO-Darwin surface-ocean layer (which is 10 m thick) over a regionally-defined deployment site from January 1995 to December 2017. Continuous experiments are performed for all five deployment sites described in Section 2.2.2.

Experiment Name	Abbreviation	Regional Bounds	Deployment Area $\times 10^3$ km^2	Experiment Type	Potential DIC Removed	$mCDR_{pot}$: Mean/Range (mol C/mol Alk)
North Atlantic	NAS	16°W–23°W	270	Continuous	10^{-2} PgC yr^{-1}	0.854
Subduction		56°N–62°N		Monthly-pulse	10^{-2} PgC	0.834–0.876
				Yearly-pulse	12×10^{-2} PgC	
Western Boundary	WBC	144°E–148°E	267	Continuous	10^{-2} PgC yr^{-1}	0.807
Current		31°N–38°N				0.792–0.826
Antarctic Circumpolar	ACC	3°E–3°W	268	Continuous	10^{-2} PgC yr^{-1}	0.876
Current		45°S–50°S		Monthly-pulse	10^{-2} PgC	0.866–0.899
				Yearly-pulse	12×10^{-2} PgC	
Equatorial Upwelling	EU	165°W–170°W	267	Continuous	10^{-2} PgC yr^{-1}	0.799
		2°S–2°N				0.783–0.811
Subtropical Gyre	STG	130°W–135°W	266	Continuous	10^{-2} PgC yr^{-1}	0.834
		30°N–35°N				0.822–0.844

Table 2. List of OAE experiments: Experiment names and their abbreviations used in this work; regional bounds oand surface area of deployment site; experiment type with respect to OAE injection duration; potential DIC removed assuming typical ocean conditions (i.e., $DIC_{tot,pot}$ from Eq. 6, assuming $mCDR_{pot} = 0.8$); and mean $mCDR_{pot}$ over the deployment site from ECCO-Darwin (temporally-averaged value over the simulation period and minimum and maximum monthly values). OAE deployment sites are shown in Figure 1.

For each of these experiments, an area-integrated alkalinity flux $\int f_A dA = 3.33 \times 10^7$ mol Alk s^{-1} is applied over a horizontal area $A \approx 270 \times 10^3$ km^2 and characteristic length scale $\sqrt{A} \approx 500$ km. The amount of deployed Alk is such that each experiment has the potential to remove $\Delta DIC_{pot} = 10^{-2}$ Pg C yr^{-1} from the atmosphere, assuming that $mCDR_{pot}$= 0.8. In reality, $mCDR_{pot}$ is not 0.8 in all of the OAE deployment regions. As discussed in Sec. 3.1, $mCDR_{pot}$ ranges from about 0.75 at the equator to 0.9 at the poles, with 0.8 being a representative global-mean value. Additionally, the true ΔDIC in each experiment will differ from the associated ΔDIC_{pot} due to ocean dynamics.

The choice of a deployment area A and OAE flux f_A are somewhat arbitrary, and the results will depend on these choices. However, we expect the results to be fairly insensitive to modest reductions or increases in the area for these multi-decade experiments because 1) the ocean tends to mix material laterally over a large area on these timescales and 2) the model grid cells are nearly 100 km wide with no capability to treat subgrid-scale plume physics and chemistry. Furthermore, the results are expected to be relatively insensitive to modest adjustments of f_A.

We note that the magnitude of ocean net CO_2 uptake, pH perturbations, and other possible environmental impacts, which will be specific to the particular OAE approach used (and might include inorganic mineral precipitation and impact on marine food web via the introduction of micro-nutrients and trace metals), are expected to be strongly correlated with the magnitude of the OAE Alk flux. In this work, we do not explore these environmental impacts in depth, as they are specific to the particular OAE approach.

2.2.4 Pulse OAE deployments

For two deployment sites associated with strong seasonality in mCDR efficiency (NAS and ACC), we performed three additional "pulse" experiments with shorter Alk deployments. Although the duration of the Alk pulse in these experiments may appear long, we stress that these timescales are fairly short compared to typical annual-to-multi-annual timescales associated with OAE-attributed net CO_2 removal (He & Tyka, 2023).

For two *monthly-pulse* experiments, OAE is applied for a duration of 31 days, starting on January 1, 1995 and July 1, 1995; these monthly-pulse experiments are termed *Jan1995* and *Jul1995* experiments, respectively. The monthly-pulse experiments were chosen because they are perceived to be the months associated with approximately minimum and maximum $mCDR_{eff}$. For these experiments, the magnitude of the Alk flux is such that each of the pulse experiment has the potential to remove 10^{-2} Pg C from the atmosphere (assuming $mCDR_{pot} = 0.8$).

For the *yearly-pulse* OAE experiments, Alk is deployed during a single year (from January 1st 1995 to December 31st 1995) and the magnitude of the Alk flux is equal to that of the monthly pulse experiments, so the potential CO_2 removed from the atmosphere is roughly 12 times larger than in each of the monthly-pulse experiments. We refer to these experiments as *Yr1995* experiments.

2.2.5 Efficiency of pulse OAE estimated from continuous experiment

In this study, we focus primarily on continuous OAE deployments, as they allow us to extract expanded insights into mCDR efficiency from each simulation compared to single pulse experiments. As shown in Zhou et al. (2025) and further demonstrated in our results, mCDR efficiencies derived from pulse experiments exhibit substantial sensitivity to the deployment month, often persisting more than a decade after the perturbation. Moreover, as discussed in Sec. 3.3.2, we demonstrate that a representative mCDR efficiency for an ensemble of pulse experiments, initiated across different months, can be effectively estimated using output from the continuous experiments and the derived metric $mCDR^{p}_{eff}$. Here we describe and schematically illustrate the relationship between pulse experiments and continuous experiments using Fig. 2.

We first consider a pulse experiment deployed over a surface-ocean area A_d instantaneously at time $t = 0$ (Fig. 2a). The net CO_2 exchange evolves on monthly to multi-annual timescales, superimposed on the background circulation-driven transport of OAE-modified waters. In Fig. 2a, a trajectory of OAE-modified waters and the corresponding values of δDIC_{tot} are shown at multiple equidistant time intervals after start of the deployment (δDIC_{tot} is the incremental increase in ocean DIC_{tot} or the net CO_2 flux integrated over the OAE-impacted area during one time increment Δt). The value of η at time $t = n\Delta t$ is calculated by summing the product of $\Delta t \cdot \delta DIC_{tot}$ over all time increments along the trajectory of OAE-perturbed waters (i.e., over Δt, $2\Delta t$, $\ldots$, $n\Delta t$) and normalizing by the product of $\Delta t \cdot \Delta Alk_{tot}$ (see Eq. 2). The value of $mCDR_{eff}$ is computed by normalizing η with the $mCDR_{pot}$ at the time of deployment (Eq. 7).

We next consider a continuous OAE experiment deployed over the same surface-ocean area A_d, starting at time $t = 0$ (Fig. 2b). This continuous deployment can be conceptualized as a series of n instantaneous incremental deployments, with each increment injecting $\delta Alk_{tot} = \Delta Alk_{tot}/n$ over successive time intervals Δt, $2\Delta t$, $\ldots$, $n\Delta t$. The value of $mCDR^{p}_{eff}$ at time $n\Delta t$, where n is the total number of time increments in the deployment, is calculated by summing δDIC_{tot} from each incremental deployment at time $n\Delta t$, normalized by the product of δAlk_{tot} and $mCDR_{pot}$ (Eq. 9). For the first pulse, normalized δDIC_{tot} is evaluated at time $n\Delta t$ after deployment, for the second increment at time $(n-1)\Delta t$, and for the last increment at time Δt after deployment. This summation accounts for multiple deployment trajectories (each corresponding to the space-time evolution of one of the incremental deployments), covering the time interval from 0 to $n\Delta t$ — this is similar to a summation of the net CO_2 flux for the pulse experiment.

In summary, $mCDR_{eff}$ time integrated in a pulse experiment is akin to integration of normalized net CO_2 flux along a single deployment trajectory, while $mCDR^{p}_{eff}$ is integrated across multiple incremental deployment trajectories. For an idealized steady-state ocean we expect the two quantities to be exactly equal. However, since the real ocean is far from steady-state, due to seasonal and interannual variability for example, $mCDR^{p}_{eff}$ represents $mCDR_{eff}$ as derived from an ensemble of back-to-back pulse experiments, each initialized to capture the variability across a representative range of space-time-evolving ocean conditions.

2.3 ECCO-Darwin Description

The ECCO-Darwin model and data assimilation methods have been extensively described in the literature (e.g., Brix et al., 2015; Manizza et al., 2019, 2023; Carroll et al., 2020, 2022; Bertin et al., 2023). In particular, a technical description of the ECCO-Darwin model set-up, observational constraints, and optimization methodology is presented in Carroll et al. (2020). In this study, we use a coarser-resolution (1° vs. 1/3° horizontal grid spacing) version of the Carroll et al. (2020) solution. Below, we provide a brief introduction to ECCO-Darwin and highlight the unique features of this model that are essential for our OAE studies.

The Lat-Lon-Cap-90 (LLC90) version of ECCO-Darwin used in this paper has 1° nominal horizontal grid spacing, spans 1992–2017, and is based on ocean circulation and

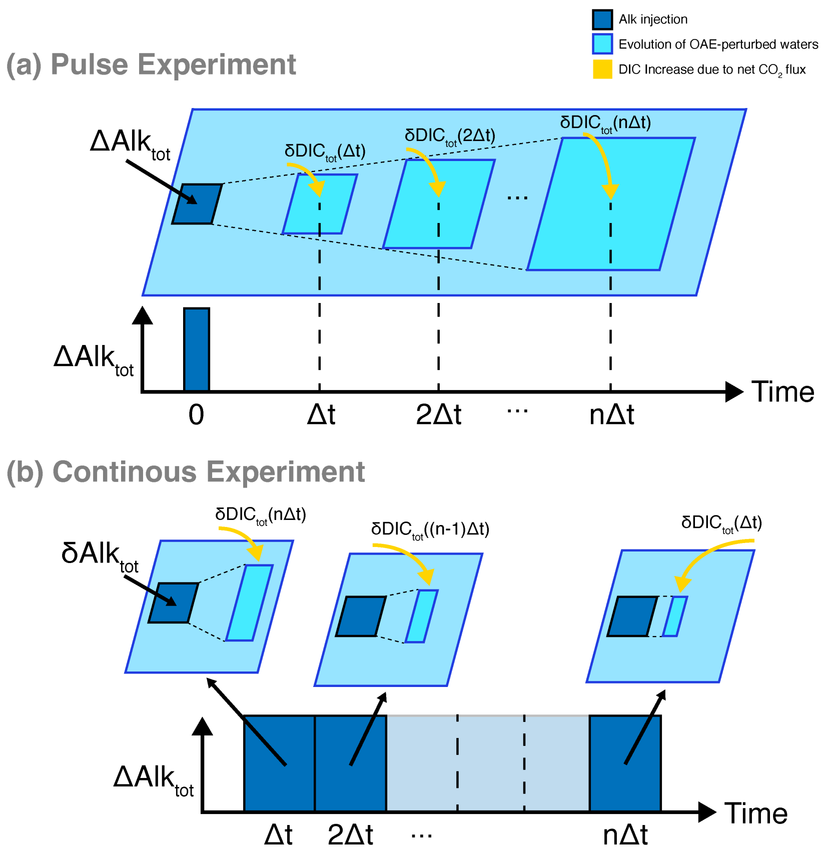

Figure 2. Schematic representing (a) a pulse OAE deployment and (b) continuous OAE deployment. Dark blue boxes represent the OAE injection area and light blue boxes represent trajectories of OAE-impacted waters across space and time; yellow arrows indicate net CO_2 uptake. δDIC and δAlk are the DIC increase due to net CO_2 flux and Alk deployment over time increment Δt.

physical tracers (i.e., temperature, salinity, and sea ice) from the Estimating the Circulation and Climate of the Ocean (ECCO) Version 4 release 4 solution (V4r4; ECCO Consortium et al., 2021; Forget, Campin, et al., 2015). Horizontal grid spacing varies from 110 km at mid-latitudes to roughly 42 km at high latitudes. The vertical grid spacing increases from 10 m near the surface to 457 m near the seafloor. Since the horizontal discretization is insufficient to resolve mesoscale eddies, their impact on large-scale ocean circulation is parameterized using the Redi (1982) and Gent and McWilliams (1990) schemes; vertical mixing is parameterized with the Gaspar et al. (1990) scheme.

The ECCO V4r4 circulation estimate is used at each time step to drive an online biogeochemistry and ecosystem model developed by the Massachusetts Institute of Technology Darwin Project (Follows et al., 2007; Dutkiewicz et al., 2015, 2020). In this version of the model, the Darwin model does not feedback on the ECCO circulation. The Darwin model includes the cycling of organic and inorganic carbon, phosphorus, iron, silica, oxygen, and alkalinity. Carbonate chemistry is based on the efficient solver of Follows et al. (2006). Air-sea CO_2 flux is computed using the parameterization of Wanninkhof (1992) and forced with atmospheric partial pressure of CO_2 from the zonally-averaged National Oceanic and Atmospheric Administration Marine Boundary Layer Reference (NOAA MBL) product (Andrews et al., 2014). The Darwin ecology includes five large-to-small phytoplankton functional types (diatoms, other large eukaryotes, Synechococcus, and low- and high-light adapted Prochlorococcus), along with two zooplankton types that graze preferentially on either large eukaryotes or small picoplankton.

Physical observations are assimilated using the adjoint method (i.e., 4-D-Var; Wunsch et al., 2009; Wunsch & Heimbach, 2013), which minimizes a weighted least squares sum of model-data misfit (i.e., a cost function) to optimize initial conditions; time-varying surface-ocean boundary conditions; and time-invariant, three-dimensional mixing coefficients for along-isopycnal, cross-isopycnal, and isopycnal thickness diffusivity. Because the initial conditions, surface boundary conditions, and mixing coefficients are estimated as part of the adjoint-method optimization, the ECCO ocean circulation estimate has negligible drift and therefore does not require spin-up. The biogeochemical model is optimized in an additional step from the circulation using a low-dimensional Green's Functions approach (Menemenlis et al., 2005) to assimilate a variety of biogeochemical observations and adjust Darwin initial conditions and ecological parameters. We neglect the first 3 years of model simulation due to biogeochemical spin-up. The LLC90 ECCO-

Darwin version closely matches the previously-published solution (Supporting Information Fig. S4).

2.4 Rapid-mCDR: 1D model for mCDR simulations

At the present time, the ECCO-Darwin simulations discussed in the previous section might be computationally too expensive for simulating and quantifying OAE efficiency, especially if a large number of OAE deployment sites and seasons are considered. To provide a numerically-efficient approach and isolate and elucidate interactions between OAE and vertical transport processes, we next develop a 1D model *rapid-mCDR* which simulates the tight coupling between OAE-modified Alk and DIC and solves for conservation equations for these quantities in Eulerian form:

$$\frac{\partial}{\partial t}\Delta\widehat{Alk} = -\frac{\partial}{\partial z}\left(\overline{w}^{*}\Delta\widehat{Alk}\right) + \frac{\partial}{\partial z}\left(\overline{K}^{*}\frac{\partial}{\partial z}\Delta\widehat{Alk}\right) + \frac{\delta_{z_k,0}}{\Delta z_1}\widehat{f_{Alk}}, \tag{10}$$

$$\frac{\partial}{\partial t}\Delta\widehat{DIC} = -\frac{\partial}{\partial z}\left(\overline{w}^{*}\Delta\widehat{DIC}\right) + \frac{\partial}{\partial z}\left(\overline{K}^{*}\frac{\partial}{\partial z}\Delta\widehat{DIC}\right) - \frac{\delta_{z_k,0}}{\Delta z_1}\Delta\widehat{f_C}, \text{and} \tag{11}$$

$$\Delta\widehat{f_C} = \overline{\kappa}^{*}(1-\overline{a}^{*}_{ice})\left(\overline{\frac{\partial p\mathrm{CO}_2^{aq}}{\partial Alk}}^{*}\Delta\widehat{Alk} + \overline{\frac{\partial p\mathrm{CO}_2^{aq}}{\partial DIC}}^{*}\Delta\widehat{DIC}\right), \tag{12}$$

where ΔDIC, ΔAlk represent OAE perturbations of DIC and Alk concentrations, and Δf_C is the net CO_2 flux from the OAE-perturbed simulation with respect to the baseline simulation. Variables w and K are 3D vertical velocity and diffusivity, κ is the piston velocity, and a_{ice} is sea-ice cover — all these variables are taken from the baseline simulation, as they are not modified by OAE in our experiments. $\widehat{\varphi}$ and $\overline{\varphi}^{*}$ represent horizontally-integrated values of φ over the global ocean and horizontally-averaged values of rapid-mCDR forcing φ over the OAE-impacted area, respectively. The value of $\delta_{z_k,0}$ is 1 for the uppermost rapid-mCDR vertical level and zero otherwise, and Δz_1 represents the ocean depth represented by that layer.

Eqs. 10 and 11 relate the time derivative of $\Delta\widehat{Alk}$ and $\Delta\widehat{DIC}$ (terms on the left hand side of these two equations) to the vertical advection and diffusion terms (first and second term on the right hand side of these equations) and prescribed Alk deployment rate or OAE-attributed net CO_2 uptake (the last terms in Equations 10 and 11, respectively). These two equations are derived by simplifying ECCO-Darwin budget equations

(Supporting Information Text S3), guided by analysis of the budget terms in the five regional-scale OAE experiments (Supporting Information Figs. S5-S6). The following two approximations are used: 1) the biological source term is neglected and 2) the products of vertical velocity and Alk perturbations are linearized as: $w\widehat{\Delta Alk} \approx \overline{w}^* \Delta\widehat{Alk}$. This approximation neglects correlation between the vertical velocity and ΔAlk over the OAE-impacted regions. A similar approximation is made for DIC and diffusion terms in the conservation equation.

Eq. 12 represents the horizontally-integrated net CO_2 flux due to OAE, which is a function of ocean-surface perturbations $\Delta\widehat{Alk}$ and $\Delta\widehat{DIC}$ and $p\mathrm{CO}_2^{aq}$ sensitivities. The $p\mathrm{CO}_2^{aq}$ sensitivities were estimated from the surface-ocean conditions in the baseline simulation using *PyCO2SYS*. The rapid-mCDR equations are solved for 50 vertical levels (which coincide with the ECCO-Darwin vertical levels) using a 1-day time step. The numerical finite difference scheme uses an implicit Euler method for time derivatives, which ensures numerical stability. A simple numerical stability analysis and sensitivity study indicates that the daily time step is sufficient (not shown). At the ocean floor, we assume net zero flux of $\Delta\widehat{Alk}$, $\Delta\widehat{DIC}$, which is used as a bottom boundary condition for Eqs. 10-11. We initialize rapid-mCDR at January 1, 1995 (before the start of OAE deployments), at which time the Alk and DIC perturbations are set to zero. Rapid-mCDR is then integrated through the ECCO-Darwin period (January 1st, 1995 to December 31st, 2017).

We note that rapid-mCDR is a 1D model that simulates vertical processes only, and therefore it does not explicitly represent the impact of horizontal transport (advection and diffusion) on OAE. Horizontal transport can however be implicitly represented by providing the required inputs for rapid-mCDR ($\overline{w}^*$, $\overline{K}^*$ and $p\mathrm{CO}_2^{aq}$ sensitivities in Equation 12) following the deployment trajectory (i.e., the space-time evolution of the OAE perturbation), which essentially "transports" the rapid-mCDR vertical column along that trajectory. In this work, rapid-mCDR inputs are taken as the spatially-averaged values over OAE-impacted regions that are defined using two distinct averaging approaches:

- *DeployAvg*: This is the simplest approach, which neglects all horizontal transport. Here rapid-mCDR inputs are averaged horizontally over the deployment site only. In this method, all OAE and DIC perturbations, as well as CO_2 uptake, are computed at the deployment site. This approach is therefore appropriate for deployment sites with relatively weak horizontal transport. Results from rapid-mCDR using this method are referred to as "rapid-mCDR(DeployAve)".

- *TransportAvg*: This approach accounts for the space-time horizontal advection and diffusion of the rapid-mCDR water column — which is driven by surface-ocean currents. In this method, ocean conditions are computed as an area-weighted mean over the region where OAE modifies surface $p\mathrm{CO}_2^{aq}$, with the weights being proportional to $\Delta p\mathrm{CO}_2^{aq}$. Results from rapid-mCDR using this approach are referred to as "rapid-mCDR(TransAve)".

3 ECCO-Darwin results

3.1 mCDR Potential

Figure 3 shows global-ocean time-mean $mCDR_{pot}$ and its climatological seasonal cycle from the ECCO-Darwin and OceanSODA-ETHZ. Time-mean $mCDR_{pot}$ reveals a pronounced meridional gradient, with the lowest values (approximately 0.75 mol C/mol Alk) located in the tropics, progressively increasing poleward and eventually exceeding 0.9 mol C/mol Alk (Fig. 3a). For the same latitudinal range, values in regions dominated by western boundary currents tend to be lower than eastern boundary currents. The amplitude of the seasonal cycle of $mCDR_{pot}$ is below 0.1 mol C/mol Alk throughout the global ocean (Figure 3b) and less than 0.05 mol C/mol Alk at the five deployment sites (Table 2). The most pronounced seasonal cycle occurs in northern mid-latitudes and polar regions, where the highest values are found in western boundary current regions, such as the Gulf Stream and Kuroshio extensions and the Brazil-Malvinas Confluence. Across the chosen five deployment sites, average $mCDR_{pot}$ from ECCO-Darwin ranges from 0.799 mol C/mol Alk (EU) to 0.854 mol C/mol Alk (NAS) (Table 2).

Following Takahashi et al. (1993), we can understand the reasons and attributes of the variability of $mCDR_{pot}$ by recognizing that its value is the negative product of DIC/Alk and $\gamma_{Alk}/\gamma_{DIC}$ (Eq. 5). The value of γ_{DIC} (the buffer or Revelle Factor) ranges from about 8 at the equator to 14 at the poles and γ_{Alk} ranges from roughly -7.4 to -13.3 (e.g. Sarmiento & Gruber, 2006), while their ratio varies comparatively little over the global ocean and seasons. Therefore, the variability of $mCDR_{pot}$ is primarily controlled by the variability of the DIC/Alk ratio, which ranges from about 0.83 at the equator to 0.94 at the poles. Due to the strong correlation between surface-ocean Alk and salinity, the

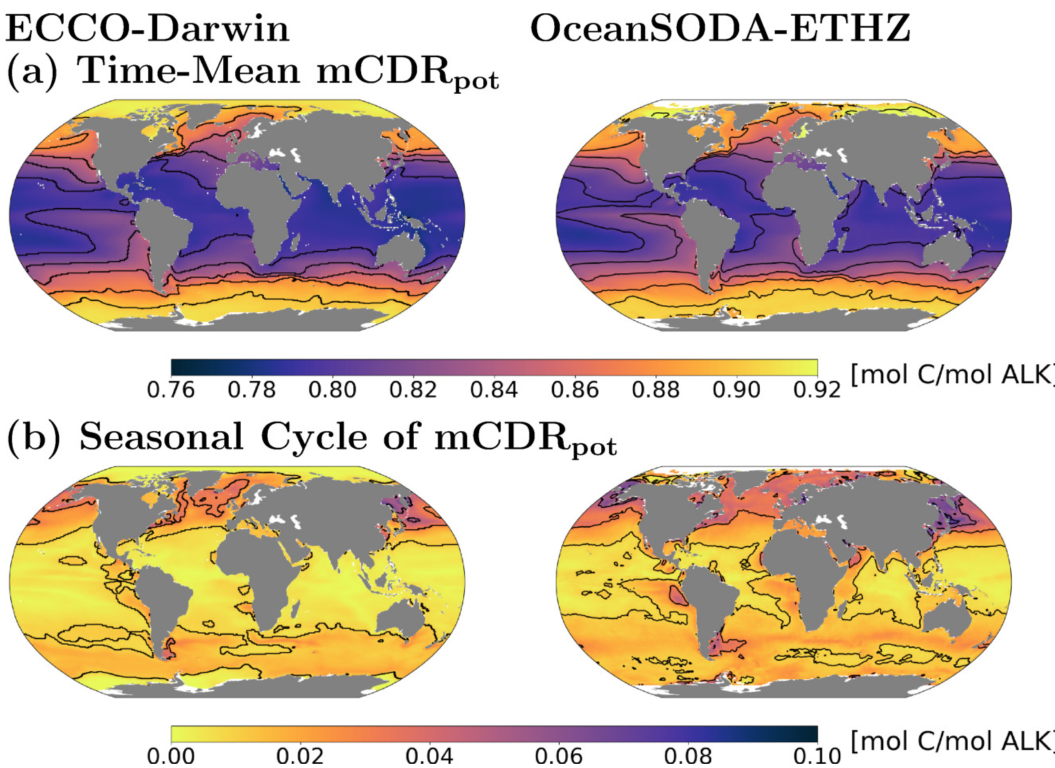

Figure 3. $mCDR_{pot}$ from the baseline ECCO-Darwin simulation (left) and OceanSODA-ETHZ dataset (right) showing (a) time-mean values over the ECCO-Darwin period (January 1995 to December 2017) and (b) magnitude of climatological seasonal cycle.

variations of surface-ocean DIC/Alk are very similar to the variations of salinity-normalized DIC and are similarly controlled by the processes other than evaporation and precipitation that affect DIC: ocean transport (circulation and mixing), biology, and air-sea flux (Takahashi et al., 1993, 2014; Gregor & Gruber, 2021).

The meridional gradient of DIC/Alk, and hence $mCDR_{pot}$, is thought to be caused by two main factors: the meridional gradient of solar heating and SST, which tends to increase surface-ocean $p\mathrm{CO}_2^{aq}$ and hence carbon outgassing at low latitudes (all else equal), as well as upwelling and entrainment of Alk- and DIC-rich waters at subpolar latitudes, which tend to enhance DIC in iron-limited regimes where biological productivity is reduced (Wu et al., 2019). The seasonal variations of $mCDR_{pot}$ are driven by a complicated variety of different combinations of air-sea CO_2 flux, ocean transport, and biology, with the latter often playing a leading role in the seasonal cycle in mid- to high-latitudes (Sarmiento & Gruber, 2006). See Carroll et al. (2022) for a recent global description of DIC dynamics derived from ECCO-Darwin.

Time-mean $mCDR_{pot}$ computed from both datasets exhibit similar features, with model-data differences generally not exceeding 0.025 mol C/mol Alk. One notable distinction is that OceanSODA-ETHZ values are marginally lower in eastern subtropical basins. Although both ECCO-Darwin and OceanSODA-ETHZ exhibit similar seasonal patterns of $mCDR_{pot}$, the seasonal cycles in OceanSODA-ETHZ tend to have larger magnitudes. Nevertheless, both ECCO-Darwin and OceanSODA-ETHZ demonstrate similar structure in $mCDR_{pot}$ suggesting it is relatively accurate in both and justifying our use of ECCO-Darwin to quantify mCDR efficiency.

In summary, the most effective OAE deployments, based solely on their potential to remove atmospheric CO_2 would be over polar oceans, provided the OAE-impacted waters were maintained at their simulated conditions throughout re-equilibration. However, in the next sections, when we consider ocean dynamics that are captured by the dynamical efficiency factor ($mCDR_{eff}$), this narrative substantially changes.

3.2 OAE impact on ocean state for continuous OAE experiments

Before quantifying OAE efficiency, we first investigate the impact of OAE on the ocean state for the five continuous experiments. These results serve as an illustration only, because the environmental impacts are expected to scale with the magnitude of deployed

Alk. We examine the spatial patterns of atmospheric CO_2 uptake and alteration of surface-ocean pH, as well as how OAE-impacted seawater mixes and subducts in the ocean interior.

For the five continuous OAE experiments, Figure 4 shows a map of time-integrated net CO_2 uptake due to OAE from the end of the ECCO-Darwin period (i.e. $\int \Delta f_c \, dt$ integrated from the January 1, 1995 to December 31, 2017). For all OAE deployments, the time-integrated net CO_2 flux is largest close to the deployment site and its footprint is indicative of near-surface horizontal advection, with the following key features:

- For NAS, the North Atlantic and the Norwegian Currents transport OAE-modified waters towards high-latitude regions, with the flow bifurcating near Iceland. As a result, the largest values of net CO_2 flux are found at, or north of the deployment site.
- For WBC and ACC, predominant zonal transport results in the largest net CO_2 flux values located primarily east of the deployment sites. In particular, the strong Antarctic Circumpolar Current in ACC spreads the net CO_2 flux eastward over a large region of the Southern Ocean.
- For EU, equatorial upwelling and upper-ocean zonal flow both north and south of the equator spread the net CO_2 flux footprint over most of the tropical/subtropical Pacific Ocean. The signature of cumulative net CO_2 flux for EU covers the largest horizontal area (not shown), while the maximum magnitude is the lowest of all 5 experiments.
- For STG, the anticyclonic circulation associated with the subtropical gyre advects OAE-impacted waters towards the southwest, spreading the net CO_2 flux footprint west of Southern California and Baja Mexico.

To illustrate the depth of the OAE perturbation across the five continuous OAE experiments, Supporting Information, Figure S8b shows the temporal evolution of the depth above which 95% of the deployed *Alk* remains. We adopt this depth threshold as a metric to demarcate OAE-modified waters from those unaffected by OAE. For all OAE experiments, the OAE perturbation spreads to deeper waters with elapsed time after deployment, with large differences occurring in the OAE perturbation depth across all experiments. By the end of the simulation, the *Alk* perturbation reaches depths in excess of 2000 m in NAS and roughly 800 m in ACC. For the other three experiments, *Alk* per-

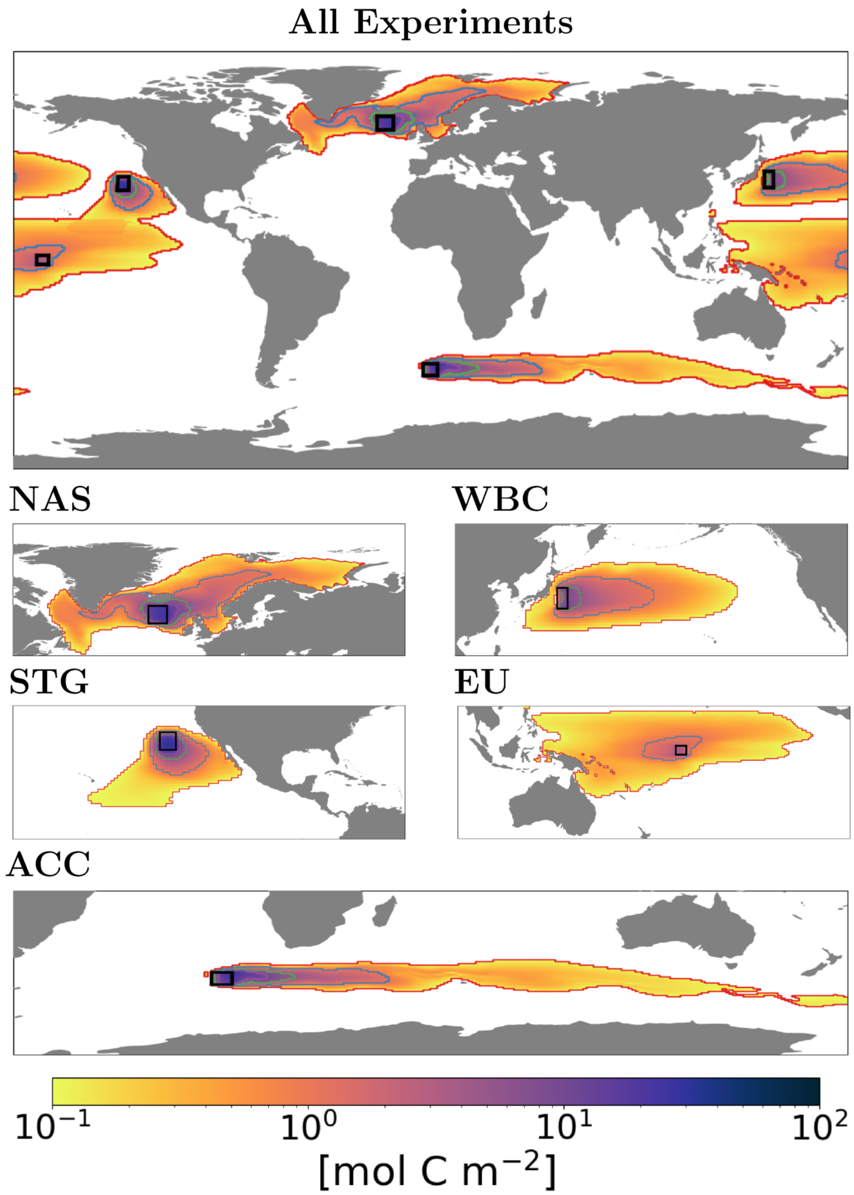

Figure 4. Time-integrated net CO_2 flux due to OAE from January 1995 to December 2017 for the 5 continuous OAE experiments. The color scale is logarithmic, highlighting variations in CO_2 uptake intensity. Isolines represent *DIC* increases of 0.1, 1, 5, 10, and 50 mol C m^{-2}. Black boxes show OAE deployment sites. Upper panel shows all 5 OAE experiments across the global ocean; lower panels show individual OAE experiments.

turbations remain much closer to the ocean surface and depths below roughly 500 m remain largely unaffected.

In Supporting Information Text S3 (and Figures S5 – S6) we also discuss horizontally-integrated budgets for DIC and Alk perturbations for the five continuous OAE experiments. These budgets separate and quantify the contributions of key processes that modify DIC and Alk perturbations. With the exception of the air-sea interface, where the DIC and Alk perturbations increase due to net CO_2 flux from the atmosphere and the prescribed Alk flux, respectively, changes to DIC and Alk perturbations are predominantly dominated by vertical ocean dynamics, while the contribution of biology is negligible.

Across all deployment sites, excluding EU, a pronounced seasonality characterizes the strength of vertical mixing and advection, coinciding with variations in mixed layer depth (MLD; Supporting Information, Figures S5 – S6). As the MLD deepens, DIC and Alk perturbations are transported into deeper waters, potentially sequestering them from the atmosphere (which inhibits or delays net CO_2 uptake) until the MLD shoals again. Notably, the relative influence of vertical advection and diffusivity (i.e., mixing) varies significantly by deployment site. The MLD and its seasonal variability differ substantially among sites, with NAS having the deepest seasonal MLD.

3.3 Efficiency of alkalinity enhancement

3.3.1 Continuous OAE experiments

For the five continuous OAE experiments, Figs. 5 and 6 show key aspects associated with net CO_2 uptake. Time series showing the total amount of deployed Alk (ΔAlk_{tot}) and potential DIC uptake and realized net DIC uptake ($\Delta DIC_{tot,pot}$ and ΔDIC_{tot}, respectively) are shown on Fig. 5. In Fig 6a, we show $mCDR_{eff}$, computed from the start of the OAE deployment (i.e., January 1, 1995) to the time shown on the x-axis. Fig. 6b shows $mCDR^{p}_{eff}$ filtered with a centered 1-year running-mean filter. The running-mean filter is applied to remove the large seasonal cycle of net CO_2 uptake. Fig. 6c shows the time-mean seasonal cycle of $mCDR^{p}_{eff}$ over the last ten years of simulation. In Supporting Information (Fig. S7) we show the time series of horizontally-averaged profiles of $mCDR_{equil}$. The deployment locations associated with large seasonality are likely related to high seasonal dependence of pulse mCDR efficiency, which we further investigate in Section 3.3.2.

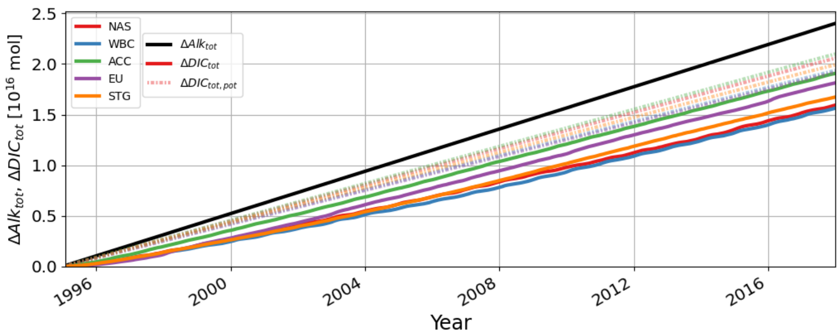

Figure 5. Continuous OAE experiment initiated on January 1, 1995. Time series of ΔAlk_{tot} (black line), ΔDIC_{tot} (solid color lines), $\Delta DIC_{tot,pot}$ (dashed colored lines). The colors represent the five different OAE deployments, as indicated by the legend.

From the perspective of potential for net CO_2 removal, the deployment locations closer to the polar regions are associated with the highest values (i.e., the highest $\Delta DIC_{tot,pot}$ in Fig. 5) as already discussed above. However, the actual net CO_2 removal (ΔDIC_{tot}) is additionally modified by the dynamical efficiency, which varies substantially among the deployment sites (Fig. 5). In all cases, ΔDIC_{tot} is considerably lower than ΔDIC_{pot} throughout the 23-year experiment, which is longer than the the air-sea adjustment timescale, indicating a strong control of ocean dynamical processes on net CO_2 removal. Fig. 5 also shows that the variability between sites in terms of $DIC_{tot,pot}$ is smaller than that of DIC_{tot}, emphasizing the critical role that variations in ocean dynamics play in driving differences in OAE efficiency across the sites.

For all continuous experiments, the dynamical efficiency ($mCDR_{eff}$) curves (Fig. 6a) increase nonlinearly with time after deployment, exhibiting the following key characteristics:

- ACC is associated with the most-rapid increase of $mCDR_{eff}$, where values exceed 0.75 within 5 years after the start of OAE and also reach one of the highest values by the end of the simulation (0.91). This is consistent with this site having the most rapid increase of $mCDR_{equil}$ in the upper ocean, as shown in Supporting Information (Fig. S7).
- For all deployments, EU is associated with the slowest initial increase of $mCDR_{eff}$, consistent with the slowest increase of $mCDR_{equil}$. However, after roughly 13 years after deployment its values reach that of the ACC and by the end of the simula-

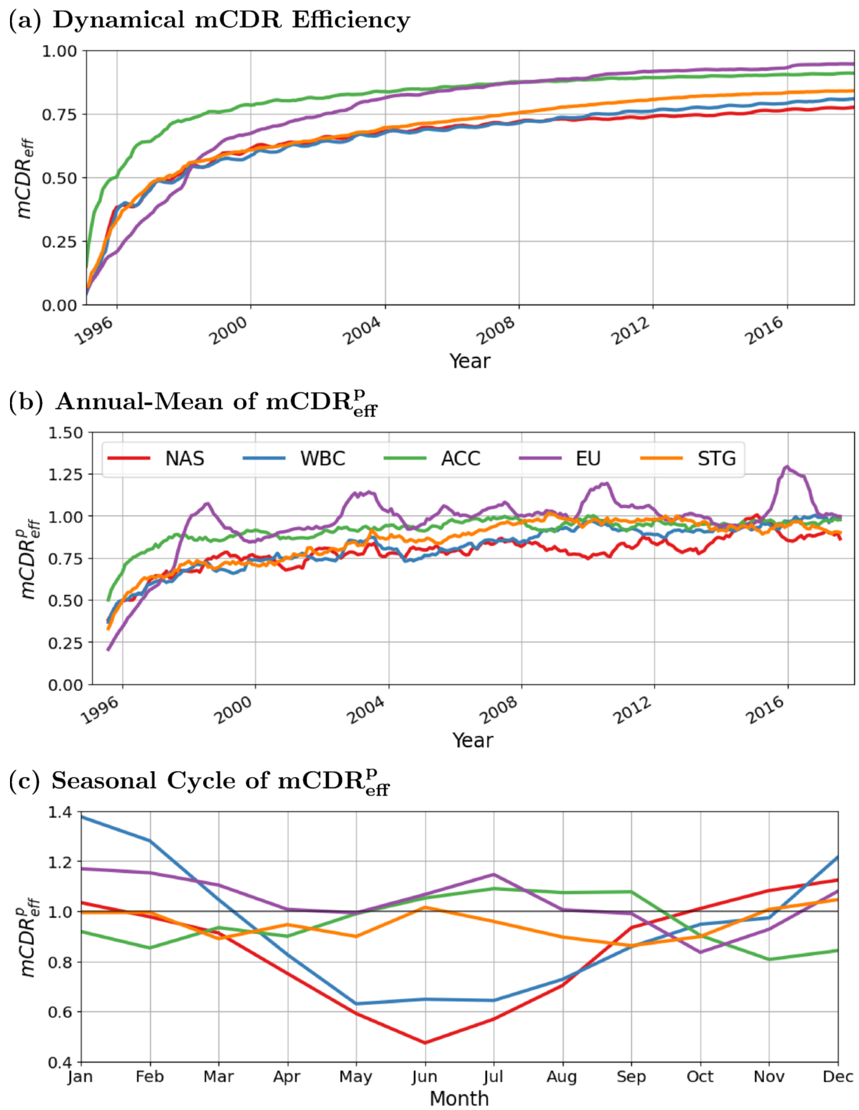

Figure 6. Continuous OAE experiment initiated on January 1, 1995 (a) Time series of dynamical mCDR efficiency; (b) Centered 1-year running-mean values of $mCDR^p_{eff}$; (c) Average seasonal cycle of $mCDR^p_{eff}$ over the last simulation decade. The colors represent the five different OAE deployments, as indicated by the legend.

tion $mCDR_{eff}$ in this region yield the highest value of all simulations, 0.95. $mCDR_{eff}$ in this region diverges from the typical shape due to strong interannual variability, which we discuss below.

- For the other three experiments (STG, WBC, and NAS), $mCDR_{eff}$ behaves remarkably similar over the first decade after deployment — by the end of 2017 their values differ by only a few percent each (0.84, 0.81, and 0.77 for STG, WBC, and NAS, respectively), despite considerable differences in the ocean dynamics of these sites.

Next we discuss the behaviour of $mCDR^p_{eff}$, as this represents the overall efficiency of the pulse experiment for the corresponding site. $mCDR^p_{eff}$ exhibits nonlinear behavior (6b) similar to that of $mCDR_{eff}$, but also highlights interannual variability. Note that for most of the experiments, $mCDR^p_{eff}$ is also associated with strong seasonality (Figure 6c), which is filtered from the timeseries shown on Figure 6b. EU exhibits the largest interannual variability in $mCDR^p_{eff}$, superimposed on the tapered nonlinear and nearly monotonic increase. This interannual variability is positively correlated with the multivariate El-Niño/Southern Oscillation (ENSO) index (Wolter & Timlin, 2011, not shown), indicating that ENSO can have a substantial impact on net CO_2 uptake in the Tropical Pacific Ocean. We note that other locations also exhibit interannual variability in $mCDR^p_{eff}$, albeit weaker than in EU. The values of running-mean $mCDR^p_{eff}$ in Fig. 6b can exceed one for a limited time period, which is most evident for the EU experiment. This does not mean that dynamical OAE efficiency exceeds 100%, rather it reflects transient mismatches in time between net CO_2 uptake and injected *Alk* flux, which are driven by ocean-atmosphere dynamics.

Figure 6c shows that $mCDR^p_{eff}$ for NAS and WBC, and to some extent ACC, are associated with a strong seasonally-dependent response of $mCDR^p_{eff}$ to the constant *Alk* flux, yielding maximum values (and thus strongest net CO_2 uptake) in winter and minimum values in summer. Peak monthly values differ from the annual-mean values by up to 40%. In ACC, the magnitude of the seasonal cycle of $mCDR^p_{eff}$ is roughly half that of NAS and is shifted in phase roughly 6 months, due to its location in the southern hemisphere.

3.3.2 Pulse OAE experiments

To understand how $mCDR_{eff}$ varies seasonally as a function of deployment month, we use three targeted pulse OAE experiments for the NAS and ACC. Each experiment uses a different OAE deployment strategy, Yr1995 (year-long pulse during 1995), Jan1995 (pulse in January 1995 only), and Jul1995 (pulse in July 1995 only), to further elucidate how $mCDR_{eff}$ depends on the season of deployment. Figure 7 shows the time series of $mCDR_{eff}$ from the pulse experiments and $mCDR^p_{eff}$ from the continuous experiments conducted at the same site, with deployment starting on January 1st, 1995.

For the three NAS experiments, the time evolution of $mCDR_{eff}$ is highly dependent on the month of Alk deployment (Figure 7a). By the end of simulation, Alk deployed in summer (Jul1995) reaches an efficiency of roughly 0.9 while the winter deployment (Jan1995) is only slightly above 0.6; the efficiency of the annual deployment (Yr1995) lies between these two extremes. Note that the seasonality in $mCDR^p_{eff}$ shown in Fig. 6 does not coincide with seasonality of $mCDR_{eff}$ for the pulse experiment.

For the NAS experiment, $mCDR^p_{eff}$ somewhat overestimates $mCDR_{eff}$ for the Yr1995 experiment, but it generally falls well between the values for Jan1995 and Jul1995 deployments, indicating that continuous virtual experiments can be used to characterize the average dynamical efficiency of an ensemble of pulse deployments distributed evenly throughout the seasonal cycle at this site. For the ACC experiments, seasonal variability in $mCDR_{eff}$ is evident during the initial years post-deployment, but after approximately ten years all experiments achieve nearly maximal dynamical efficiency (Figure 7b). Overall, the results at two sites in Figure 7 are suggestive that $mCDR^p_{eff}$ may be a reasonable approximation of the ensemble-average efficiency of pulse deployments.

We emphasize that the seasonality of $mCDR^p_{eff}$, which is discussed in Sec. 3.3.1, is likely related to, yet distinct from, the seasonality of $mCDR_{eff}$ observed in the pulse experiments. The first quantifies the seasonally-dependent response of net CO_2 flux to constant Alk forcing and the latter quantifies the response of net CO_2 flux to seasonally-dependent Alk injection.

4 Rapid-mCDR results

In this section, we first compare the two versions of rapid-mCDR against ECCO-Darwin and discuss the difference in results when using the two spatial averaging meth-

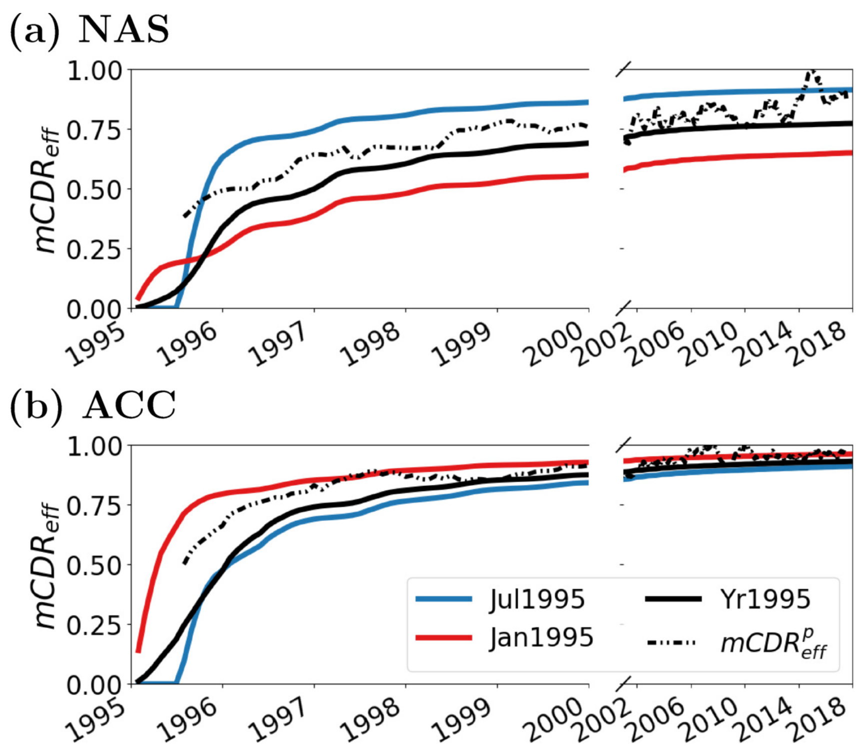

Figure 7. $mCDR_{eff}$ for monthly-pulse experiments (blue and red lines) and yearly-pulse experiments (black lines) and $mCDR^{p}_{eff}$ for continuous experiment shown as centered 1-year running-mean values (black dashed line); (a) NAS and (b) ACC.

ods to approximate the impact of horizontal transport described in Section 2.4. Then as an example use case, we use rapid-mCDR to understand how and why mCDR efficiency varies latitudinally across a meridional section of the central Pacific Ocean.

4.1 Evaluation of rapid-mCDR against ECCO-Darwin for the 5 OAE deployments

Figure 8 evaluates $mCDR^{p}_{eff}$ from rapid-mCDR simulations against ECCO-Darwin across all five continuous OAE experiments. As discussed in Sec. 2.4, we expect rapid-mCDR(TransAve) to better reproduce ECCO-Darwin than rapid-mCDR(DeployAve) due to its more accurate representation of horizontal transport. Although the primary output of rapid-mCDR is net CO_2 uptake, here we show different aspects of $mCDR^{p}_{eff}$, including:

1. Scatter plots of monthly-mean $mCDR^{p}_{eff}$ from ECCO-Darwin and the two rapid-mCDR versions. These provide a measure of the overall skill of rapid-mCDR in emulating CO_2 uptake efficiency (left panel).
2. Time series of $mCDR^{p}_{eff}$ using a 1-year centered-running mean, showing the bias in rapid-mCDR simulations (middle panel).
3. Seasonal cycle of $mCDR^{p}_{eff}$, further indicating the skill of rapid-mCDR and seasonal bias (right panel).

Supporting Information Fig. S7 illustrates the agreement in $mCDR_{equil}$ between ECCO-Darwin and the two rapid-mCDR versions, highlighting the consistent vertical Alk and DIC transport between the two models.

For NAS, the $mCDR^{p}_{eff}$ from rapid-mCDR(TransAve) agrees well with ECCO-Darwin for the entire duration of the experiment (Fig. 8a). The coefficient of determination for the monthly-mean values of $mCDR^{p}_{eff}$ is $R^2 = 0.9$. The rapid-mCDR(TransAve) slightly underestimates annual-mean values of $mCDR^{p}_{eff}$ during the first part of the simulation, but this underestimation is less than 0.05. The seasonal cycle of $mCDR^{p}_{eff}$ is well simulated by this version of rapid-mCDR. The rapid-mCDR(DeployAve) somewhat overestimates $mCDR^{p}_{eff}$ during most of the simulation period, except for the first five years after the start of deployment (Fig. 8a). While this overestimation is primarily due to the winter months, as revealed by comparison of the seasonal cycle, the overestimation remains present to some degree throughout the year. The winter overestimation is likely dominated by the absence of sea ice for rapid-mCDR(DeployAve), which impacts both ECCO-Darwin and rapid-mCDR(TransAve). The spatial average of sea-ice area over the impacted region in ECCO-Darwin can reach up to 0.15 in the winter period (not shown), which is expected to reduce winter CO_2 uptake (and therefore $mCDR^p_{eff}$) by roughly that fraction. Despite the degradation in the rapid mCDR solution due to ignoring horizontal transport in rapid-mCDR(DeployAve), the coefficient of determination $R^2 = 0.67$ and the time-mean bias are relatively modest.

For WBC, both versions of rapid-mCDR closely represent ECCO-Darwin, with only a modest overestimation of the annual-mean values of $mCDR^p_{eff}$, and rapid-mCDR(TransAve) providing a somewhat better match to ECCO-Darwin (Fig. 8b). This agreement holds for both the time series of annual-mean values and the coefficients of determination, which are $R^2 = 0.90$ for rapid-mCDR(TransAve) and $R^2 = 0.76$ for rapid-mCDR(DeployAve). Furthermore, the seasonal cycles from both rapid-mCDR versions generally align well with that of ECCO-Darwin. A similar level of performance or rapid-mCDR is observed for ACC, as shown in Fig.8c.

For EU, the agreement of $mCDR^p_{eff}$ between ECCO-Darwin and the two rapid-mCDR simulations is the poorest of all five OAE experiments, with $R^2 = 0.74$ for rapid-mCDR(TransAve) and $R^2 = 0.03$ for rapid-mCDR(DeployAve) (Fig. 8d). The annual-mean comparison shows that rapid-mCDR(DeployAve) is unable to sufficiently represent interannual variability, which is large in this location. rapid-mCDR(TransAve) represents this interannual variability better, likely due to the fact that it approximates horizontal transport and thus the dispersal of OAE-impacted waters better. Nevertheless, the mean bias averaged over the seasonal and interannual variability is relatively modest for both approaches.

In STG, rapid-mCDR(DeployAve) significantly underestimates $mCDR^p_{eff}$ approximately a decade after the start of deployment, while rapid-mCDR(TransAve) agrees better with ECCO-Darwin ($R^2 = 0.31$ and 0.88, respectively). The cause of this underestimation is likely similar to the EU deployment, where after a number of years OAE-impacted waters spread across a large region, which the rapid-mCDR(DeployAve) approach does not capture.

In Figure 9 we demonstrate the ability of rapid-mCDR to represent mCDR efficiency for the three pulse experiments for NAS and ACC, which were previously shown

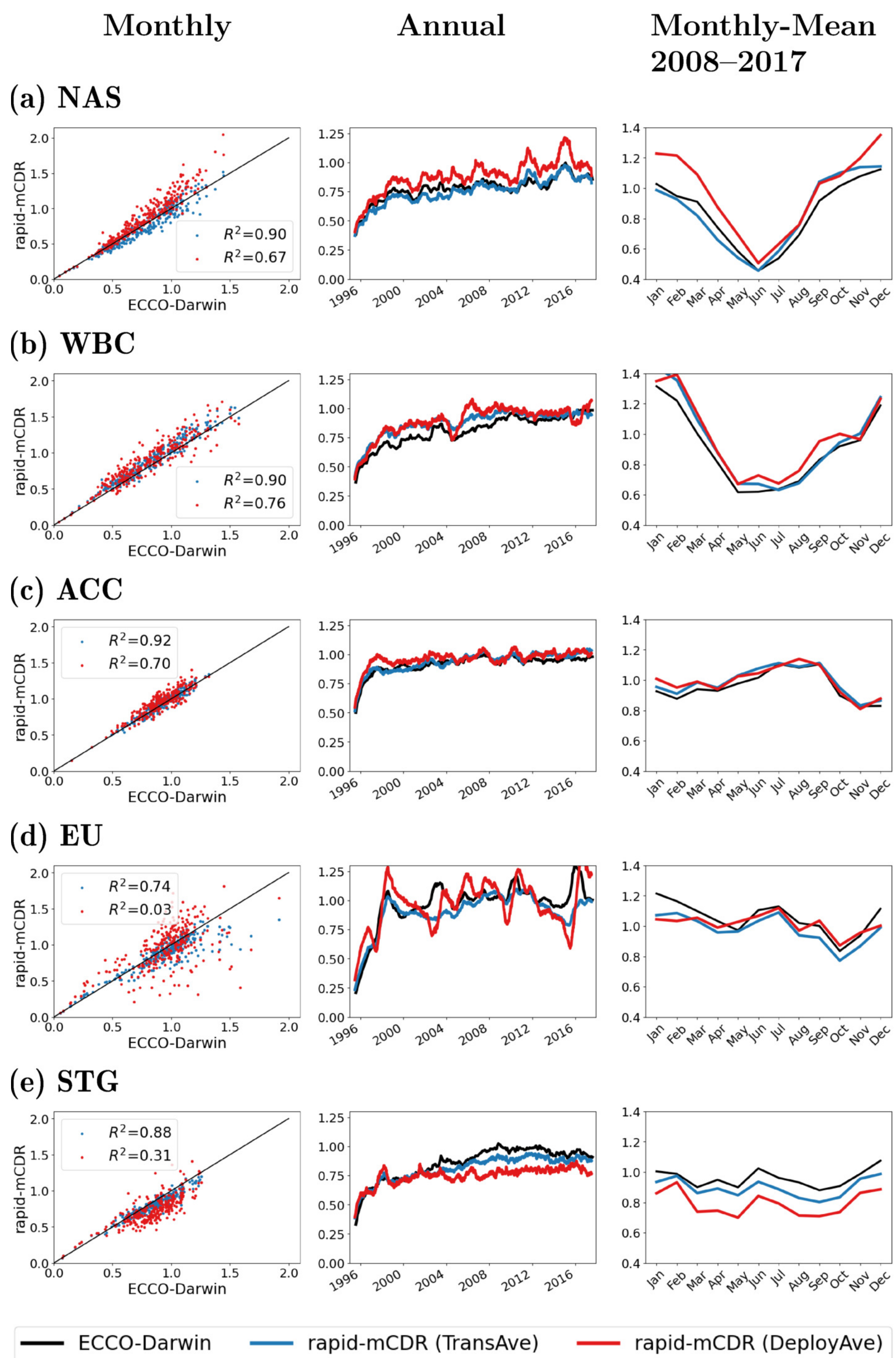

Figure 8. Comparison of $mCDR^{p}_{eff}$ from ECCO-Darwin and both versions of rapid-mCDR. Left panels (a–e) show monthly-mean ECCO-Darwin vs. rapid-mCDR, along with associated R^2 values. Middle panels show time series using a 1-year centered-running mean; right panels show monthly-mean values to provide a zoom-in period during the last 10 years of simulation. Blue and red lines represent rapid-mCDR(TransAve) and rapid-mCDR(DeployAve), respectively. Black line in middle and right panels shows ECCO-Darwin.

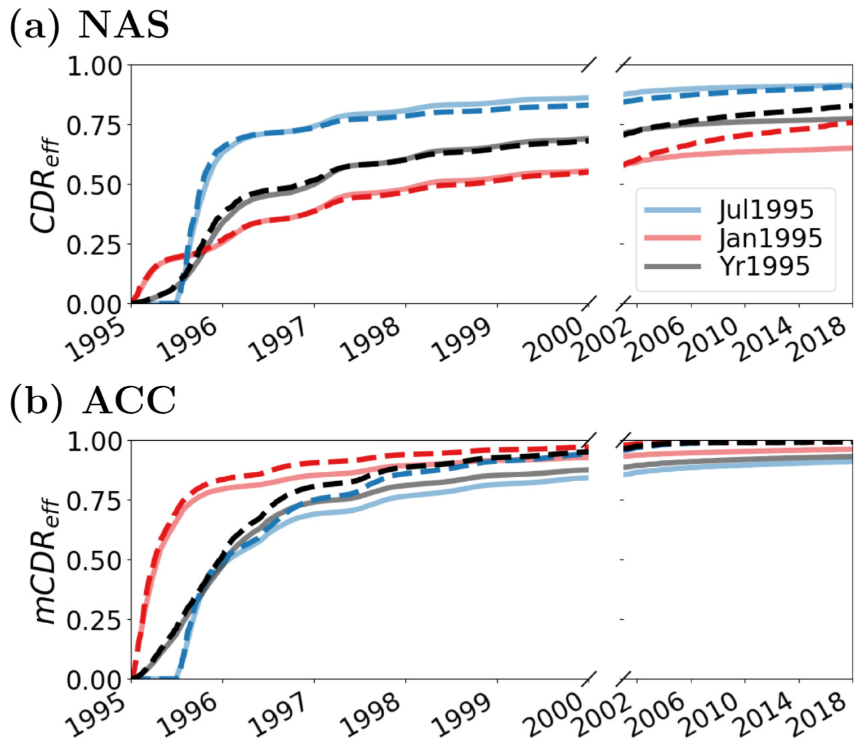

Figure 9. $mCDR_{eff}$ for monthly-pulse and yearly-pulse experiments in (a) NAS and (b) ACC. Solid lines show ECCO-Darwin, dashed lines show rapid-mCDR(TransAve).

to strongly vary with deployment season. Here, only results from rapid-mCDR(TransAve) are shown. For NAS, rapid-mCDR agrees well with ECCO-Darwin over the first five years after deployment and shows some skill in representing seasonally-varying $mCDR_{eff}$, as discussed above. However, by the end of the simulation rapid-mCDR somewhat overestimates $mCDR_{eff}$; this overestimation is consistent for all three experiments. For ACC, $mCDR_{eff}$ is overestimated by rapid-mCDR — a result that is consistent with the continuous OAE experiments in this region. Rapid-mCDR predicts that by the end of the simulation $mCDR_{eff}$ approaches a value of one, which is roughly 0.1 larger than ECCO-Darwin. Overall, despite its simplicity, rapid-mCDR generally reproduces the results of ECCO-Darwin.

4.2 Expanding rapid-mCDR to ocean-basin scales

In this section, we provide an example use case of rapid-mCDR to characterize dynamical mCDR efficiency ($mCDR_{eff}$) across space-time scales that might be prohibitively expensive to examine with ECCO-Darwin. We also use rapid-mCDR to isolate the physical processes (such as sea-ice cover or vertical mixing) that reduce $mCDR_{eff}$ by analyzing the model's response to modifications in the strength of these processes. This approach would be challenging with ECCO-Darwin, as altering the strength of such processes in the numerical ocean model could cause unintended downstream effects in the simulated fields.

We simulate *Alk* deployment across the meridional extent of the Pacific Ocean, centered on 165°W, with deployments spaced 1° apart in latitude from 77°S to 52°N. This latitudinal range is chosen so that each deployment represents open-ocean conditions. Each deployment covers a rectangular area 10° in longitude by 3° in latitude; the central deployment locations are shown in Fig. 10a. For all of these deployments, we use rapid-mCDR(DeployAve) where the inputs are taken from the baseline ECCO-Darwin simulation. At each deployment location, we perform three experiments, corresponding to the three ECCO-Darwin pulse experiments discussed in Section 2.2.4: *Yr1995*, *Jul1995*, and *Yr1995*. As with ECCO-Darwin, these experiments are run until December 31, 2017 and the $mCDR_{eff}$ values are evaluated at the end of simulation (roughly 23 years after deployment).

Furthermore, to isolate the effects of physical processes (vertical advection, vertical diffusivity, and sea-ice cover) on $mCDR_{eff}$, we performed three additional sets of sensitivity experiments based on the Yr1995 experiment described above with the following modifications: 1) *Yr1995-w0* is an experiment with vertical velocity set to zero, 2) *Yr1995-k0* is an experiment with vertical diffusivity set to zero, and 3) *Yr1995-ice0* is an experiment with no sea-ice cover (i.e., purely open-water conditions).

Figure 10b shows $mCDR_{eff}$ for the Yr1995 experiment at the end of simulation, plotted against the central latitude of each deployment location, along with profiles of time-mean vertical velocity and vertical diffusivity. Figure 10c shows profiles of normalized *Alk* perturbation (i.e., $\Delta\widehat{Alk}$ normalized by the maximum value of all experiments) at the end of simulation to show the vertical extent of the OAE perturbation.

We find that $mCDR_{eff}$ is strongly dependent on deployment location (Fig. 10b), with the largest values found near the equator, at subpolar latitudes in the southern hemisphere (between approximately 60–50°S), and at mid-latitudes in the northern hemisphere (between approximately 40–50°N). The lowest values (less than 0.5) are generally found in subtropical regions and near the poles. High $mCDR_{eff}$ values generally coincide with upwelling regions (Fig. 10b), where Alk perturbations remain near the surface (Fig. 10c). Low $mCDR_{eff}$ values are associated with downwelling regions for which the Alk perturbations are either transported to depth or spread over a substantial vertical extent (Fig. 10b-c).

Figure 11 shows $mCDR_{eff}$ for the three deployment seasons (Figure 11a) and three sensitivity experiments (Figure 11b). For reference, Figure 11c shows $mCDR_{pot}$ and sea-ice cover. All quantities are plotted as a function of deployment latitude. We find that $mCDR_{eff}$ has a strong dependence on deployment season in the mid-latitudes and subtropics. Summer months are generally associated with higher efficiency compared to winter, which is consistent with the pulse experiments for NAS and ACC (see Section 3.3). The $mCDR_{eff}$ is up to 0.3 higher in summer compared to winter, which is also consistent with the seasonality of $mCDR_{eff}$ for the NAS pulse experiments (Sec. 3.3.2).

We also find that sea-ice cover strongly suppresses $mCDR_{eff}$. The experiments shown in Figure 11b demonstrate that for polar OAE deployments in the southern hemisphere, which are under the influence of seasonal sea ice, the sea-ice cover prevents CO_2 uptake and therefore these regions are associated with low values of $mCDR_{eff}$. Removing sea-ice cover in rapid-mCDR (Figure 11b, orange line) increases $mCDR_{eff}$ to values close to one south of roughly 50°S. Therefore, our simulations suggest that mCDR efforts will be much less efficient in this and other sea-ice-covered regions.

From the two dominant ocean circulation processes, vertical velocity and diffusivity, we find that vertical velocity dominates low-efficiency regions. That is, the vertical diffusivity is of secondary importance. There is only a small increase of $mCDR_{eff}$ with respect to the Yr1995 experiment if the vertical diffusivity is set to zero (Figure 11b, purple line). However, if the vertical velocity is set to zero $mCDR_{eff}$ becomes close to one for most of the deployment sites (Figure 11b, green line), except for sea-ice-covered regions in the southern hemisphere.

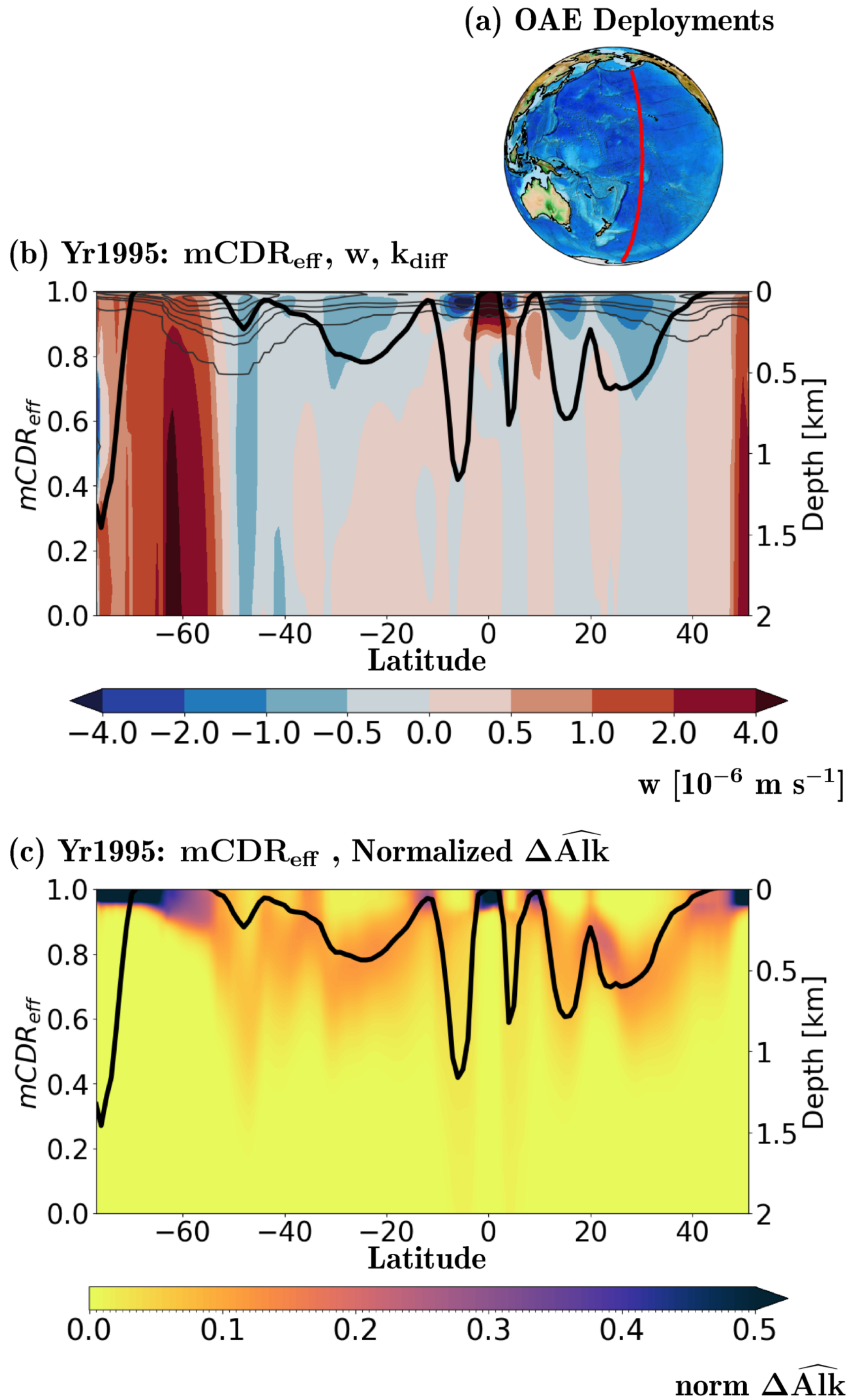

Figure 10. (a) Location of rapid-mCDR deployments across the Pacific Ocean; (b) $mCDR_{eff}$ at the end of 2017 for Yr1995 experiment (solid black line), profile of average vertical velocity (colored contours), and vertical diffusivity (gray contour lines with units of 10^{-2} m^2 s^{-1}); (c) $mCDR_{eff}$ at the end of 2017 for Yr1995 experiment (solid black line) and Alk perturbation normalized by the maximum value of all experiments ($\Delta\widehat{Alk}$; colored contours).

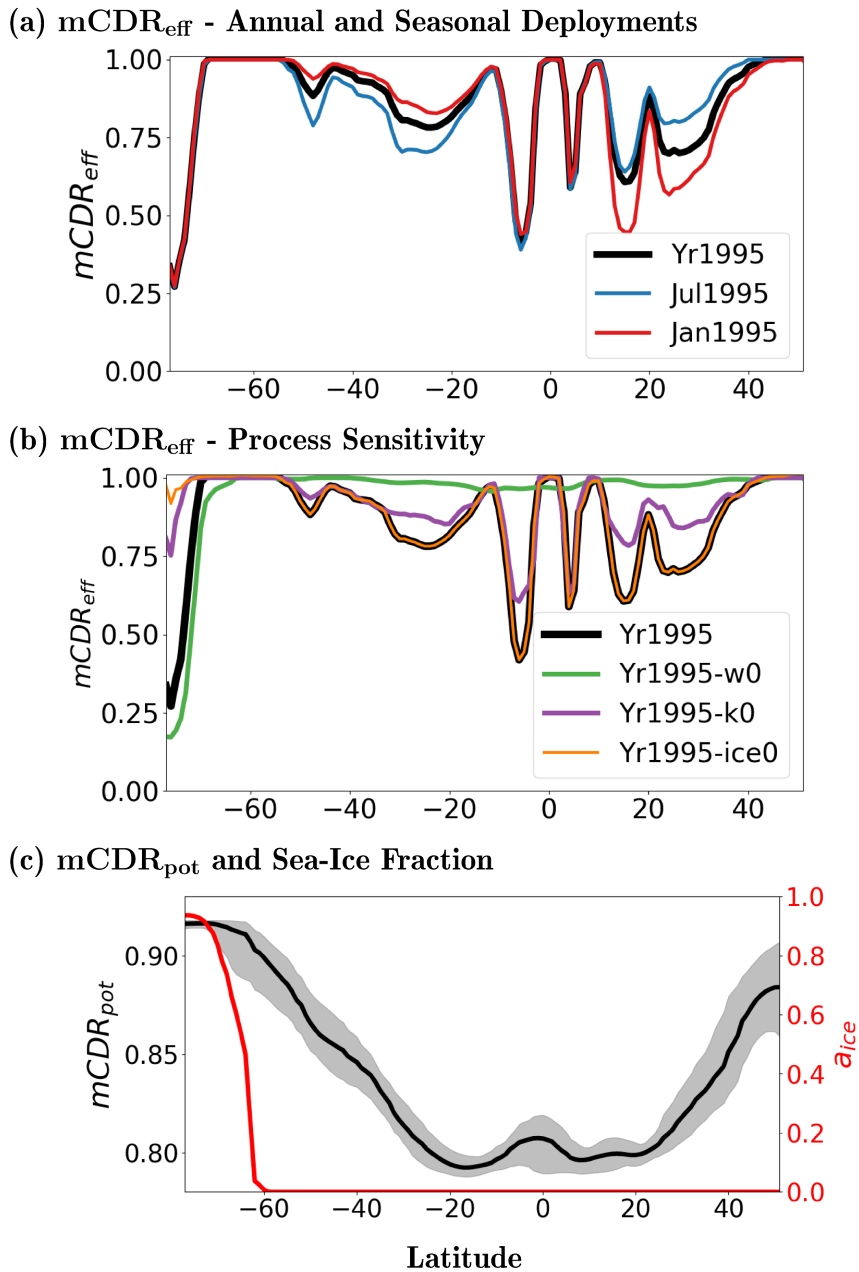

Figure 11. Pacific Ocean vertical sections of $mCDR_{eff}$ at the end of 2017 for (a) 3 different pulse deployment seasons (Jul1995, Jan1995, and Yr1995). (b) Experiments with vertical velocity and diffusivity set to zero (Yr1995-w0 and Yr1995-k0, respectively) and simulation without sea-ice forcing (Yr1995-ice0). (c) Average $mCDR_{pot}$ and variability over the deployment site (solid black lines and gray shading, respectively); these are computed from daily-mean values and time-mean sea-ice cover. All values are taken from and shown at the central latitude of the deployment location.

5 Summary and Discussion

ECCO-Darwin is an open-source, data-constrained ocean model designed to integrate physical and biogeochemical processes in a dynamically-consistent framework. Its use of adjoint-based data assimilation for physical processes enables the model to fit global-ocean observations without relying on non-physical nudging or incremental adjustments (Forget, Fukumori, et al., 2015; Carroll et al., 2020). This approach preserves the internal consistency of ocean physics and biogeochemistry, allowing for fully-closed budgets of conserved properties, which is an essential capability for mechanistic studies and attribution of carbon fluxes in mCDR research. Furthermore, ECCO-Darwin's ability to constrain both circulation and biogeochemistry with observations enhances confidence in its simulation of ocean dynamics and carbon cycling, making it especially well suited for evaluating the efficacy and impacts of mCDR strategies.

In this work, we designed a series of virtual ECCO-Darwin OAE deployments to investigate variability of mCDR efficiency (i.e. the normalized net CO_2 uptake) across archetypal ocean circulation regimes. For two representative regions (i.e. in the North Atlantic subpolar gyre and over the Antarctic Circumpolar Current; NAS and ACC) we compare mCDR efficiency with similar experiments from a different model described by Zhou et al. (2025) (Supporting Material, Figure S9). In both regions, ECCO-Darwin simulates higher mCDR efficiencies, with the largest difference observed in the NAS. This may reflect ECCO-Darwin's data-constrained treatment of vertical mixing, mixed layer depth (MLD), and the air-sea disequilibrium ($p\mathrm{CO}_2^{aq}$), which are critical to OAE outcomes. Further inter-model comparisons are needed to better understand the processes driving mCDR efficiency and to identify sources of uncertainty across modeling frameworks.

While our results offer valuable insight into the variability of mCDR efficiency across major open-ocean circulation regimes, several key limitations remain, alongside opportunities for targeted improvements. To more accurately represent specific OAE deployments, future work should incorporate critical biogeochemical interactions between OAE materials and seawater, including mineral dissolution and precipitation processes (e.g., Fennel et al., 2023). Simulating mineral-based deployments and tracking their dissolution products (e.g., Si and Fe) is also important due to potential ecological impacts (Bach et al., 2019). In polar regions, more realistic representations of air-sea CO_2 exchange—particularly through sea-ice cracks and leads—could improve flux estimates (Loose & Schlosser, 2011; Søren et al., 2011). Our current experiments are limited to open-ocean conditions and do not account for coastal environments. Accurately capturing nearshore OAE deployments will likely require high-resolution regional models or unstructured grid approaches capable of resolving coastal, estuarine, and near-source dynamics (Ward et al., 2020).

We use our ECCO-Darwin results to motivate and develop a user-friendly 1D model, rapid-mCDR, for rapid quantification of net CO_2 uptake and mCDR efficiency. Users can simulate virtual OAE deployments in various ocean conditions without the need for supercomputing resources — which is a key advantage compared to more complex ECCO-Darwin simulations. Combining the 1D model approach with already-published output from a numerical ocean biogeochemistry model, such as ECCO-Darwin (see the Open Research Section), permits characterization of mCDR efficiency for any OAE deployment. Although rapid-mCDR is a simplified model, it reproduces ECCO-Darwin mCDR experiments relatively well, with the exception of the deployment location in the Tropical Pacific equatorial upwelling (EU). At the two deployment sites (NAS and ACC), the discrepancies between ECCO-Darwin and rapid-mCDR are smaller than those between ECCO-Darwin and Zhou et al. (2025). The rapid-mCDR model is complementary to the impulse response function approach of Zhou et al. (2025); Yankovsky et al. (2024), as it can provide more insight into the process drivers and can be better tailored to specific OAE deployment strategies.

Future rapid-mCDR enhancements will focus on improving the representation of horizontal transport, especially in tropical regions, through either Eulerian or Lagrangian approaches (Lange & van Sebille, 2017; Delandmeter & van Sebille, 2019), as our results indicate that the horizontal transport significantly modulates mCDR efficiency for these regions, which can be seen from the difference between the results of the two versions, rapid-mCDR(DeployAve) and rapid-mCDR(TransAve) for the EU deployment. Furthermore, we are developing a module for mCDR uncertainty quantification using Monte-Carlo approaches. We envision that rapid-mCDR will be a valuable tool for rapid early-stage evaluation of potential OAE deployments, as well as for projecting OAE efficiency under future climate scenarios.

Open Research Section

ECCO-Darwin model output is available at the ECCO Data Portal: `http://data.nas.nasa.gov/ecco/`

Model code and platform-independent instructions for running ECCO-Darwin and rapid-mCDR simulations are available at: https://doi.org/10.5281/zenodo.10562714

Acknowledgments

A portion of this research was carried out at the Jet Propulsion Laboratory, California Institute of Technology, under a contract with the National Aeronautics and Space Administration (80NM0018D0004). Support from the NASA Carbon Monitoring Systems (CMS) and Ocean Biology & Biogeochemistry programs are acknowledged. High-end computing resources were provided by the NASA Advanced Supercomputing (NAS) Division of the Ames Research Center. Government sponsorship is acknowledged. We would like to express our gratitude to the two anonymous reviewers and the editor for their valuable feedback and insightful comments, which have greatly improved the quality of this manuscript.

References

Andrews, A. E., Kofler, J. D., Trudeau, M. E., Williams, J. C., Neff, D. H., Masarie, K. A., ... Tans, P. P. (2014). CO_2, CO, and CH_4 measurements from tall towers in the NOAA Earth System Research Laboratory's Global Greenhouse Gas Reference Network: instrumentation, uncertainty analysis, and recommendations for future high-accuracy greenhouse gas monitoring efforts. *Atmospheric Measurement Techniques*, *7*(2), 647–687.

Bach, L. T., Gill, S. J., Rickaby, R. E. M., Gore, S., & Renforth, P. (2019). CO_2 Removal With Enhanced Weathering and Ocean Alkalinity Enhancement: Potential Risks and Co-benefits for Marine Pelagic Ecosystems. *Frontiers in Climate*, *1*.

Bertin, C., Carroll, D., Menemenlis, D., Dutkiewicz, S., Zhang, H., Matsuoka, A., ... Le Fouest, V. (2023). Biogeochemical River Runoff Drives Intense Coastal Arctic Ocean CO_2 Outgassing. *Geophysical Research Letters*, *50*(8), e2022GL102377. doi: 10.1029/2022GL102377

Brix, H., Menemenlis, D., Hill, C. N., Dutkiewicz, S., Jahn, O., Wang, D., ... Zhang, H. (2015). Using Green's Functions to initialize and adjust a global, eddying ocean biogeochemistry general circulation model. *Ocean Modelling*, *95*, 1–14.

Burt, D. J., Fröb, F., & Ilyina, T. (2021). The sensitivity of the marine carbonate system to regional ocean alkalinity enhancement. *Frontiers in Climate*, *3*.

Carroll, D., Menemenlis, D., Adkins, J. F., Bowman, K. W., Brix, H., Dutkiewicz, S., ... Zhang, H. (2020). The ECCO-Darwin Data-Assimilative Global Ocean Biogeochemistry Model: Estimates of Seasonal to Multidecadal Surface Ocean pCO_2 and Air-Sea CO_2 Flux. *Journal of Advances in Modeling Earth Systems*, *12*(10), 1–28.

Carroll, D., Menemenlis, D., Dutkiewicz, S., Lauderdale, J. M., Adkins, J. F., Bowman, K. W., ... Zhang, H. (2022). Attribution of space-time variability in global-ocean dissolved inorganic carbon. *Global Biogeochemical Cycles*, *36*(3), e2021GB007162.

Carroll, D., Menemenlis, D., Zhang, H., Mazloff, M., McKinley, G., Fay, A., ... Fenty, I. (2024, February). *Evaluation of the ECCO-Darwin Ocean Biogeochemistry State Estimate vs. In-situ Observations.* Zenodo. Retrieved from https://doi.org/10.5281/zenodo.10627664 doi: 10.5281/zenodo.10627664

Danabasoglu, G., Yeager, S. G., Bailey, D., Behrens, E., Bentsen, M., Bi, D., ... others (2014). North atlantic simulations in coordinated ocean-ice reference experiments phase ii (core-ii). part i: mean states. *Ocean Modelling*, *73*, 76–107.

Delandmeter, P., & van Sebille, E. (2019). The Parcels v2.0 Lagrangian framework: new field interpolation schemes. *Geoscientific Model Development*, *12*(8), 3571–3584. doi: 10.5194/gmd-12-3571-2019

Dutkiewicz, S., Cermeno, P., Jahn, O., Follows, M. J., Hickman, A. E., Taniguchi, D. A. A., & Ward, B. A. (2020). Dimensions of marine phytoplankton diversity. *Biogeosciences*, *17*(3), 609–634.

Dutkiewicz, S., Hickman, A. E., Jahn, O., Gregg, W. W., Mouw, C. B., & Follows, M. J. (2015). Capturing optically important constituents and properties in a marine biogeochemical and ecosystem model. *Biogeosciences*, *12*(14), 4447–4481.

ECCO Consortium, Fukumori, I., Wang, O., Fenty, I., Forget, G., Heimbach, P., & Ponte, R. M. (2021). *ECCO SBO Core Products - Snapshot (Version 4 Release 4b).* NASA Physical Oceanography Distributed Active Archive Center. Retrieved from `https://podaac.jpl.nasa.gov/dataset/ECCO_L4_SBO_CORE_TIME_SERIES_SNAPSHOT_V4R4B` (see Product Usage section under PODAAC Documentation tab) doi: 10.5067/ECTSS-SBO4B

Eisaman, M. D., Geilert, S., Renforth, P., Bastianini, L., Campbell, J., Dale, A. W., ... Rønning, J. (2023). Assessing the technical aspects of ocean-alkalinity-enhancement approaches. *State of the Planet*, *2-oae2023*, 3.

England, M. H. (1995). The age of water and ventilation timescales in a global ocean model. *Journal of Physical Oceanography*, *25*(11), 2756–2777.

Fennel, K., Long, M. C., Algar, C., Carter, B., Keller, D., Laurent, A., ... Whitt, D. B. (2023). Modelling considerations for research on ocean alkalinity enhancement (OAE). *State of the Planet*, *2-oae2023*, 1–29. doi: 10.5194/sp-2-oae2023-9-2023

Follows, M. J., Dutkiewicz, S., Grant, S., & Chisholm, S. W. (2007). Emergent Biogeography of Microbial Communities in a Model Ocean. *Science*, *315*(5820), 1843–1846.

Follows, M. J., Ito, T., & Dutkiewicz, S. (2006). On the solution of the carbonate chemistry system in ocean biogeochemistry models. *Ocean Modelling*, *12*(3), 290–301.

Forget, G., Campin, J.-M., Heimbach, P., Hill, C. N., Ponte, R. M., & Wunsch, C. (2015). ECCO version 4: an integrated framework for non-linear inverse modeling and global ocean state estimation. *Geoscientific Model Development*, *8*(10), 3071–3104.

Forget, G., Fukumori, I., Heimbach, P., Lee, T., Menemenlis, D., & Ponte, R. M. (2015). Estimating the Circulation and Climate of the Ocean (ECCO): Advancing CLIVAR Science. *CLIVAR Exchanges*, *67*(19), 41–45.

Friedlingstein, P., Jones, M. W., O'Sullivan, M., Andrew, R. M., Bakker, D. C. E., Hauck, J., ... Zeng, J. (2022). Global carbon budget 2021. *Earth System Science Data*, *14*(4), 1917–2005.

Gaspar, P., Grégoris, Y., & Lefevre, J.-M. (1990). A simple eddy kinetic energy model for simulations of the oceanic vertical mixing: Tests at station Papa and long-term upper ocean study site. *Journal of Geophysical Research: Oceans*, *95*(C9), 16179-16193.

Gent, P. R., & McWilliams, J. C. (1990). Isopycnal mixing in ocean circulation models. *Journal of Physical Oceanography*, *20*(1), 150–155.

González, M. F., Ilyina, T., Sonntag, S., & Schmidt, H. (2018). Enhanced rates of regional warming and ocean acidification after termination of large-scale ocean alkalinization. *Geophysical Research Letters*, *45*(14), 7120–7129.

Gregor, L., & Gruber, N. (2021). OceanSODA-ETHZ: a global gridded data set of the surface ocean carbonate system for seasonal to decadal studies of ocean acidification. *Earth System Science Data*, *13*(2), 777–808.

Griffies, S. M., Biastoch, A., Böning, C., Bryan, F., Danabasoglu, G., Chassignet, E. P., ... others (2009). Coordinated ocean-ice reference experiments (cores). *Ocean modelling*, *26*(1-2), 1–46.

Gruber, N., Clement, D., Carter, B. R., Feely, R. A., van Heuven, S., Hoppema, M., ... Wanninkhof, R. (2019). The Oceanic Sink for Anthropogenic CO_2 from 1994 to 2007. *Science*, *363*(6432), 1193–1199.

He, J., & Tyka, M. D. (2023). Limits and CO_2 equilibration of near-coast alkalinity enhancement. *Biogeosciences*, *20*, 27–43.

House, K. Z., House, C. H., Schrag, D. P., & Aziz, M. J. (2007). Electrochemical acceleration of chemical weathering as an energetically feasible approach to mitigating anthropogenic climate change. *Environmental Science & Technology*, *41*(24), 8464-8470. doi: 10.1021/es0701816

Humphreys, M. P., Lewis, E. R., Sharp, J. D., & Pierrot, D. (2022). PyCO2SYS v1.8: marine carbonate system calculations in Python. *Geoscientific Model Development*, *15*(1), 15–43.

Ilyina, T., Wolf-Gladrow, D., Munhoven, G., & Heinze, C. (2013). Assessing the potential of calcium-based artificial ocean alkalinization to mitigate rising atmospheric CO_2 and ocean acidification. *Geophysical Research Letters*, *40*(22), 5909–5914.

IPCC. (2022). *Climate change 2022: Mitigation of climate change. contribution of working group iii to the sixth assessment report of the intergovernmental panel on climate change* (P. Shukla et al., Eds.). Cambridge, UK and New York, NY, USA: Cambridge University Press. doi: 10.1017/9781009157926

Jones, D. C., Ito, T., Takano, Y., & Hsu, W.-C. (2014). Spatial and seasonal variability of the air-sea equilibration timescale of carbon dioxide. *Global Biogeochemical Cycles*, *28*(11), 1163–1178.

Lange, M., & van Sebille, E. (2017). Parcels v0.9: prototyping a Lagrangian ocean analysis framework for the petascale age. *Geoscientific Model Development*, *10*(11), 4175–4186. doi: 10.5194/gmd-10-4175-2017

Loose, B., & Schlosser, P. (2011). Sea ice and its effect on CO_2 flux between the atmosphere and the Southern Ocean interior. *Journal of Geophysical Research: Oceans*, *116*(C11). doi: 10.1029/2010JC006509

Manizza, M., Carroll, D., Menemenlis, D., Zhang, H., & Miller, C. E. (2023). Modeling the Recent Changes of Phytoplankton Blooms Dynamics in the Arctic Ocean. *Journal of Geophysical Research: Oceans*, *128*(6), e2022JC019152. doi: 10.1029/2022JC019152

Manizza, M., Menemenlis, D., Zhang, H., & Miller, C. E. (2019). Modeling the Recent Changes in the Arctic Ocean CO_2 Sink (2006–2013). *Global Biogeochemical Cycles*, *33*(3), 420–438.

Menemenlis, D., Fukumori, I., & Lee, T. (2005). Using Green's Functions to Calibrate an Ocean General Circulation Model. *Monthly Weather Review*, *133*(5), 1224–1240.

Middelburg, J. J., Soetaert, K., & Hagens, M. (2020). Ocean alkalinity, buffering and biogeochemical processes. *Reviews of Geophysics*, *58*(3), e2019RG000681.

Montserrat, F., Renforth, P., Hartmann, J., Leermakers, M., Knops, P., & Meysman, F. J. R. (2017). Olivine Dissolution in Seawater: Implications for CO_2 Sequestration through Enhanced Weathering in Coastal Environments. *Environ. Sci. Technol.*(7), 3960–3972.

National Academies of Sciences, Engineering, and Medicine. (2022). *A Research Strategy for Ocean-based Carbon Dioxide Removal and Sequestration.* Washington, DC: The National Academies Press. doi: 10.17226/26278

Palter, J., Cross, J., Long, M., Rafter, P., & Reimers, C. (2023). The science we need to assess marine carbon dioxide removal. *Eos*, *104*.

Redi, M. H. (1982). Oceanic isopycnal mixing by coordinate rotation. *Journal of Physical Oceanography*, *12*(10), 1154–1158.

Renforth, P., & Henderson, G. (2017). Assessing ocean alkalinity for carbon sequestration. *Reviews of Geophysics*, *55*(3), 636-674.

Rogelj, J., Popp, A., Calvin, K. V., Luderer, G., Emmerling, J., Gernaat, D., ... Tavoni, M. (2018). Scenarios towards limiting global mean temperature increase below 1.5°C. *Nature Climate Change*, *8*(4), 325–332.

Sarmiento, J., & Gruber, N. (2006). *Ocean biogeochemical dynamics*. Princeton University Press.

Schimel, D. S., & Carroll, D. (2024). Carbon cycle–climate feedbacks in the post-paris world. *Annual Review of Earth and Planetary Sciences*, *52*(1), null. doi: 10.1146/annurev-earth-031621-081700

Søren, R., Bendtsen, J., Delille, B., Dieckmann, G. S., Glud, R. N., Kennedy, H., ... Tison, J.-L. (2011). Sea ice contribution to the air–sea CO2 exchange in the Arctic and Southern Oceans. *Tellus B: Chemical and Physical Meteorology*, *63*(5), 823–830. doi: 10.1111/j.1600-0889.2011.00571.x

Takahashi, T., Broecker, W., Werner, S. R., & Bainbridge, A. (1980). Carbonate chemistry of the surface waters of the world oceans. *Isotope marine chemistry*, 291–326.

Takahashi, T., Olafsson, J., Goddard, J. G., Chipman, D. W., & Sutherland, S. (1993). Seasonal variation of co2 and nutrients in the high-latitude surface oceans: A comparative study. *Global Biogeochemical Cycles*, *7*(4), 843–878.

Takahashi, T., Sutherland, S. C., Chipman, D. W., Goddard, J. G., Ho, C., Newberger, T., ... Munro, D. (2014). Climatological distributions of pH, pCO_2, total CO_2, alkalinity, and $CaCO_3$ saturation in the global surface ocean, and temporal changes at selected locations. *Marine Chemistry*, *164*, 95–125.

Taylor, L. L., Quirk, J., Thorley, R. M. S., Kharecha, P. A., Hansen, J., Ridgwell, A., ... Beerling, D. J. (2016). Enhanced weathering strategies for stabilizing climate and averting ocean acidification. *Nature Clim Change*, *6*, 402–406.

Treguier, A. M., de Boyer Montégut, C., Bozec, A., Chassignet, E. P., Fox-Kemper, B., McC. Hogg, A., ... others (2023). The mixed-layer depth in the ocean model intercomparison project (omip): impact of resolving mesoscale eddies. *Geoscientific Model Development*, *16*(13), 3849–3872.

Tsujino, H., Urakawa, L. S., Griffies, S. M., Danabasoglu, G., Adcroft, A. J., Amaral, A. E., ... others (2020). Evaluation of global ocean–sea-ice model simulations based on the experimental protocols of the ocean model intercomparison project phase 2 (omip-2). *Geoscientific Model Development*, *13*(8), 3643–3708.

Tyka, M. D. (2024). Efficiency metrics for ocean alkalinity enhancement under responsive and prescribed atmosphere conditions. *EGUsphere*, *2024*, 1–18. Retrieved from https://egusphere.copernicus.org/preprints/2024/egusphere-2024-2150/ doi: 10.5194/egusphere-2024-2150

Tyka, M. D., Van Arsdale, C., & Platt, J. C. (2022). CO_2 capture by pumping surface acidity to the deep ocean. *Energy Environ. Sci.*, *15*(2), 786–798. doi: 10.1039/D1EE01532J

Wang, H., Pilcher, D. J., Kearney, K. A., Cross, J. N., Shugart, O. M., Eisaman, M. D., & Carter, B. R. (2023). Simulated impact of ocean alkalinity enhancement on atmospheric CO_2 removal in the Bering Sea. *Earth's Future*, *11*(1), e2022EF002816.

Wanninkhof, R. (1992). Relationship between wind speed and gas exchange over the ocean. *Journal of Geophysical Research: Oceans*, *97*(C5), 7373–7382.

Ward, N. D., Megonigal, J. P., Bond-Lamberty, B., Bailey, V. L., Butman, D., Canuel, E. A., … Windham-Myers, L. (2020). Representing the function and sensitivity of coastal interfaces in earth system models. *Nature Communications*, *11*(1), 2458.

Williams, R. G., & Follows, M. J. (2011). *Ocean dynamics and the carbon cycle: Principles and mechanisms.* Cambridge University Press.

Wolter, K., & Timlin, M. S. (2011). El Niño/Southern Oscillation behaviour since 1871 as diagnosed in an extended multivariate ENSO index (MEI.ext). *International Journal of Climatology*, *31*(7), 1074–1087. doi: 10.1002/joc.2336

Wu, Y., Hain, M. P., Humphreys, M. P., Hartman, S., & Tyrrell, T. (2019, July). What drives the latitudinal gradient in open-ocean surface dissolved inorganic carbon concentration? *Biogeosciences*, *16*(13), 2661–2681. doi: 10.5194/bg-16-2661-2019

Wunsch, C., & Heimbach, P. (2013). Dynamically and kinematically consistent global ocean circulation and ice state estimates. In G. Siedler, S. M. Griffies, J. Gould, & J. A. Church (Eds.), *Ocean circ. clim. a 21st century perspect.* (Vol. 103, pp. 553–579). New York, NY: Academic Press.

Wunsch, C., Heimbach, P., Ponte, R., & Fukumori, I. (2009). The Global General Circulation of the Ocean Estimated by the ECCO-Consortium. *Oceanography*, *22*(2), 88–103.

Yamamoto, K., DeVries, T., & Siegel, D. A. (2024). Metrics for quantifying the efficiency of atmospheric CO_2 reduction by marine carbon dioxide removal (mcdr). *Environmental Research Letters*, *19*(10), 104053.

Yankovsky, E., Zhou, M., Tyka, M., Bachman, S., Ho, D., Karspeck, A., & Long, M. (2024). Impulse response functions as a framework for quantifying ocean-based carbon dioxide removal. *EGUsphere*, *2024*, 1–26.

Zeebe, R. E., & Wolf-Gladrow, D. (2001). *Co$_2$ in seawater: equilibrium, kinetics, isotopes* (No. 65). Gulf Professional Publishing.

Zhou, M., Tyka, M. D., Ho, D. T., Yankovsky, E., Bachman, S., Nicholas, T., ... Long, M. C. (2025). Mapping the global variation in the efficiency of ocean alkalinity enhancement for carbon dioxide removal. *Nature Climate Change*, *15*(1), 59–65.

Supporting Information for "Regional Efficiency of Marine Carbon Removal via Alkalinity Enhancement: Insights from ECCO-Darwin and a 1D Model"

Kay Suselj[1], Dustin Carroll[2,1], Daniel Whitt[3], Bridget Samuels[4], Dimitris Menemenlis[1], Hong Zhang[1], Nate Beatty[5], Anna Savage[5]

[1]Jet Propulsion Laboratory, California Institute of Technology, Pasadena, CA, USA

[2]Moss Landing Marine Laboratories, San José State University, Moss Landing, CA, USA

[3]NASA Ames Research Center, Moffett Field, CA, USA

[4]Clima-Tek Analytics LLC, Pasadena, CA

[5]Running Tide, Inc., Portland, ME, USA

Contents of this file

Text S1. Validation of Baseline ECCO-Darwin Simulation.

Fig. S1 compares key time-mean surface-ocean fields that impact mCDR potential from the baseline ECCO-Darwin simulation against reference datasets. This comparison highlights the essential ocean conditions characterized by both chemical and physical/dynamical processes and provides the evidence that ECCO-Darwin credibly represents the processes crucial for simulating OAE. Reference sea-surface temperature (SST) is derived from optimally-interpolated satellite and in-situ observations using the methodology of Reynolds, Rayner, Smith, Stokes, and Wang (2002). Sea-surface salinity (SSS), dissolved inorganic carbon (DIC), and Alk are from the OceanSODA-ETHZ dataset (Gregor & Gruber, 2021), which leverages a suite of observations and a two-step approach (cluster-regression) to construct gridded monthly-mean fields that represent the global-ocean carbonate system.

The key aspects of ECCO-Darwin shown on Figure S1 are as follows:

- Polarward decrease of SST as well as the zonal gradient observed across ocean basins (Figure S1a). The latter feature is attributed to meridional transport by large-scale ocean gyres.

- Polarward decrease of SSS and Alk and maximum values located in subtropical regions associated with high rates of evaporation (Figure S1b,d). The lowest values are located in regions that exhibit significant sea-ice melt and/or intense precipitation.

- Poleward increase of DIC with significant hemispheric asymmetry. The lowest DIC values are generally found in the tropics, which are associated with increased biological productivity resulting from by upwelling-driven nutrient supply (Figure S1c).

Figure S2 compares key surface-ocean variables from the previously-published ECCO-Darwin LLC 270 solution (Carroll et al., 2020) against the LLC90 ECCO-Darwin version used in this work. The agreement between the two solutions shows that there is no need for further parameter tuning in the LLC90 set-up.

Figure S3 shows the OAE deployment location and time-mean values of surface magnitude of horizontal velocity, vertical velocity and vertical diffusivity. These fields provide the background ocean state onto which OAE is applied.

Figure S4 shows additional validation for the 5 OAE locations: a scatter-plots of DIC and Alk profile from baseline ECCO-Darwin simulations against in-situ GLODAPv2.2022 observations (Olsen et al., 2020) at the 5 deployment sites studied in this work. For all five locations, both DIC and Alk from ECCO-Darwin generally reproduce observations, which demonstrates that ECCO-Darwin captures the key biogeochemical variables relevant for OAE studies in these regions.

Text S2. Estimation of mCDR potential.

We estimate $mCDR_{pot}$ following its definition and considering the full carbon chemistry, as:

$$mCDR_{pot} = \frac{\partial DIC}{\partial Alk} \approx \frac{DIC(pCO_2^{aq}, Alk + \delta Alk, SST, SSS) - DIC(pCO_2^{aq}, Alk, SST, SSS)}{\delta Alk}, \tag{1}$$

where DIC is taken as a function of $p\mathrm{CO}_2^{aq}$, Alk , sea surface temperature (SST), and sea surface salinity (SSS), and is estimated using the *PyCO2SYS* (Humphreys et al., 2022) carbonate system. In this computation, the concentration of borate and minor ions are taken to be a function of salt concentration, as it is usually done. We take

$\delta Alk = 100$ μmol kg^{-1}. The results are not sensitive to the exact value of δAlk and we use the monthly-mean values of the surface- ocean state.

In this approach, $mCDR_{pot}$ can thus be estimated from the baseline state of the ocean (without considering the specific OAE approach) from ECCO-Darwin or any other dataset that include required inputs for Equation 1.

In this work, we estimate $mCDR_{pot}$ from both the baseline ECCO-Darwin and OceanSODA-ETHZ (Gregor & Gruber, 2021) datasets.

Text S3. Budgets of DIC and Alk perturbations due to OAE

To quantify vertical mixing and dynamics of Alk and DIC perturbations and their interaction with OAE-attributed net CO_2 uptake, we derive horizontally averaged equations for Alk and DIC perturbations, as described below. We begin with the budget equations for these two quantities as represented in ECCO-Darwin (Carroll et al., 2022):

$$\frac{\partial DIC}{\partial t} = -\nabla(\vec{u} \cdot DIC) + \nabla K(\nabla DIC) + \frac{\partial DIC}{\partial t}\Big|_{bio} + \frac{\partial DIC}{\partial t}\Big|_{dillution} + \frac{\partial f_C}{\partial z}\ , \quad (2)$$

$$\frac{\partial Alk}{\partial t} = -\nabla(\vec{u} \cdot Alk) + \nabla K(\nabla Alk) + \frac{\partial Alk}{\partial t}\Big|_{bio} + \frac{\partial Alk}{\partial t}\Big|_{dillution} + \frac{\partial f_A}{\partial z}, \quad (3)$$

where symbols $\vec{u}$ and K are the 3-D velocity and diffusivity fields.

The terms on the left-hand-side of Equations 2 and 3 represent tendency terms. The first two terms on the right-hand-side of the two equations are resolved advection and parameterized turbulent and molecular diffusion, the third term (with the subscript *bio*) represents biological impacts, and the fourth term (with the subscript *dillution*) represents dilution due to freshwater flux through precipitation and river runoff, and the last terms represent the air-sea CO_2 exchange and Alk flux for DIC and Alk , respectively.

Next, we horizontally integrate Equations 2 and 3 over the global ocean and compute the difference of the budget terms for the OAE-perturbed and baseline simulation to obtain the following two equations for DIC and Alk perturbations:

$$\underbrace{\frac{\partial}{\partial t}\widehat{\Delta DIC}}_{\text{tendency}} = \underbrace{-\frac{\partial}{\partial z}\widehat{w\Delta DIC}}_{\text{advection}} + \underbrace{\frac{\partial}{\partial z}\widehat{K\frac{\partial}{\partial z}\Delta DIC}}_{\text{diffusion}} + \underbrace{\frac{\partial}{\partial t}\widehat{\Delta DIC|_{bio}}}_{\text{biology}} + \underbrace{\frac{\partial}{\partial z}\widehat{\Delta f_C}}_{CO_2\text{ flux}} \text{ and} \tag{4}$$

$$\underbrace{\frac{\partial}{\partial t}\widehat{\Delta Alk}}_{\text{tendency}} = \underbrace{-\frac{\partial}{\partial z}\widehat{w\Delta Alk}}_{\text{advection}} + \underbrace{\frac{\partial}{\partial z}\widehat{K\frac{\partial}{\partial z}\Delta Alk}}_{\text{diffusion}} + \underbrace{\frac{\partial}{\partial t}\widehat{\Delta Alk|_{bio}}}_{\text{biology}} + \underbrace{\frac{\partial}{\partial z}\widehat{\Delta f_A}}_{\text{OAE }\Delta Alk}, \tag{5}$$

where Alk and DIC perturbations between OAE and baseline simulations are represented by ΔAlk and ΔDIC, respectively and the $\widehat{\varphi}$ represents the horiontal integral of variable φ over the global ocean. To derive Equations 4 and 5, we assume that ocean circulation and Alk/DIC dilution are not impacted by the OAE deployment, and that for advective and diffusive terms the horizontal components become zero.

For the 5 continuousAlk experiments, Figs. S5 and S6 show the profiles of budget terms for $\Delta\widehat{DIC}$ and $\Delta\widehat{Alk}$. For all of the OAE deployments the response of biological processes was insignificant — the biological source terms were at least 3 orders of magnitude lower compared to the tendency terms for both $\Delta\widehat{DIC}$ and $\Delta\widehat{Alk}$ and are therefore not shown. For clarity, the budget terms are shown only for the last 5 years of simulation; however, they are representative of the entire simulation period.

In addition, Figs S5 and S6 show the mixed layer depth (MLD) as indicative of the interface that separates highly turbulent and relatively well-mixed near-surface layer from the stably-stratified ocean below. The MLD is diagnosed from daily averaged values of thermodynamic fields, and since there is considerable uncertainty in characterization of

MLD we plot its values from *Boyer* (de Boyer Montégut et al., 2004), *Suga* (Suga & Hanawa, 1990), and *Kara* (Kara et al., 2003) methods.

For the NAS deployment, MLD varies most strongly and is between 400–900-m deep during winter and early spring and shoals to about 50-m during summer. The three MLD depth computations differ, especially during winter and early spring when the MLD is deepest. Boyer and Suga MLD differ the most, with Boyer being consistently shallower, while Kara MLD lies between these two extremes. For NAS, vertical diffusion transports $\Delta\widehat{DIC}$ and $\Delta\widehat{Alk}$ from the surface via a deepening of the MLD, which indicates presence of strong vertical mixing. This transport is strongest when the MLD deepens substantially during winter. Vertical advection transports near-surface $\Delta\widehat{DIC}$ and $\Delta\widehat{Alk}$ into upper-ocean layers (roughly 100-m deep), while it is also responsible for a sink of $\Delta\widehat{DIC}$ and $\Delta\widehat{Alk}$ throughout much of the deeper layer between 200–800 m. This advective transport appears to be fairly independent of MLD dynamics. The tendency of near-surface $\Delta\widehat{Alk}$ exhibits a strong seasonal cycle: $\Delta\widehat{Alk}$ generally increases when the MLD shoals (due to OAEAlk addition). However, when the MLD deepens, even though theAlk is added in the near surface layer, the $\Delta\widehat{Alk}$ decreases at the expense of vertical mixing associated with a deepening of the MLD. Similar dynamics occur for $\Delta\widehat{DIC}$, except that the $\Delta\widehat{DIC}$ budget is impacted by atmospheric CO_2 which also has a strong seasonal cycle peaking in late fall and early winter — just before the MLD begins to deepen.

WBC, ACC, and STG sites share many similar characteristics, except that for ACC the MLD is out of phase because the deployment is located in the southern hemisphere. MLD dynamics are dominated by strong seasonality and deepen to roughly 200 m during spring and are shallowest during late summer for the respective hemispheres. For EU, the

MLD has weaker seasonality. The three MLD criteria agree well in terms of MLD depth and seasonal variability. As for NAS, the deepening of the MLD is associated with strong vertical diffusion of $\Delta\widehat{DIC}$ and $\Delta\widehat{Alk}$ from the surface within the MLD. Here vertical diffusion tend to overshoot the MLD and indicates either underestimation of MLD by all three MLD criterion or strong vertical mixing that extends beyond the MLD. For both of these locations, advection transports both $\Delta\widehat{Alk}$ and $\Delta\widehat{DIC}$ from near-surface waters to depth. While ACC has weak seasonality in advective transport, it is substantial for WBC. As for NAS, surface-ocean $f\mathrm{CO}_2$ has strong seasonality, which is presumably related to the seasonality of MLD and advective term. This seasonality is less apparent for ACC and STG. We note that the seasonality of $f\mathrm{CO}_2$ can also be impacted by CO_2 piston velocity.

For EU, due to its location in the tropics, has no discernible seasonal cycle of MLD. Here diffusion generally mixes $\Delta\widehat{Alk}$ and $\Delta\widehat{DIC}$ from the surface downwards and advection, while it exhibit significant temporal variations, generally transports $\Delta\widehat{Alk}$ and $\Delta\widehat{DIC}$ towards the surface. This site also has seasonal transport of $\Delta\widehat{Alk}$ and $\Delta\widehat{DIC}$ below 150-m depth. EU is associated with strong multi-annual variability in $p\mathrm{CO}_2^{aq}$. For the 5-year shown in Figure S5, the $p\mathrm{CO}_2^{aq}$ is significantly increased around the start of year 2016.

Text S4. Additional comparison of ECCO-Darwin and rapid-mCDR

While the main comparison of ECCO-Darwin against rapid-mCDR is shown in the main text, Figure S7 shows additional comparison of vertically-resolved $mCDR_{equil}$ between ECCO-Darwin and rapid-mCDR, along with its time evolution for all five continuous experiments and for both both versions of horizontal averaging (rapid-mCDR(DeployAve) and rapid-mCDR(TransAve) see main text for details).

For all five experiments, rapid-mCDR generally captures the ECCO-Darwin profiles of $mCDR_{equil}$. In general, we find that the values with rapid-mCDR(TransAve) are closer to ECCO-Darwin compared to values from rapid-mCDR(DeployAve) which is expected as the former ones accounts for the horizontal advection of OAE perturbation.

Text S5. Additional figures

For the five continuous OAE experiments, Figure S8a shows the maximum pH modification due to OAE for all five continuous experiments and the time series of the depth that separates OAE-impacted waters from unmodified waters, and Figure S8b shows the time series of the depth that separated OAE-impacted waters from unmodified waters (see main text for definition and details).

Figure S9 compares the net CO_2 uptake efficiency, η, from monthly and yearly NAS and ACC deployments in ECCO-Darwin to the range of efficiencies derived from the four closest polygons in Zhou et al. (2025), obtained from the CarbonPlan website[1]. The specific polygons used for this comparison are listed in Table S1. For this comparison, we assume that the deployments in Zhou et al. (2025) were conducted in the year 1995. To estimate the yearly deployment efficiency, we averaged efficiency values from four representative months: January, April, July, and October.

As shown in Figure S9, the overall efficiency η is higher in ECCO-Darwin. However, the seasonal variation in efficiency is comparable between the two simulations. Further investigation is needed to attribute these differences to the underlying processes.

References

Carroll, D., Menemenlis, D., Adkins, J. F., Bowman, K. W., Brix, H., Dutkiewicz, S., . . . Zhang, H. (2020). The ECCO-Darwin Data-Assimilative Global Ocean Biogeochemistry Model: Estimates of Seasonal to Multidecadal Surface Ocean pCO_2 and Air-Sea CO_2 Flux. *Journal of Advances in Modeling Earth Systems*, *12*(10), 1–28.

Carroll, D., Menemenlis, D., Dutkiewicz, S., Lauderdale, J. M., Adkins, J. F., Bowman, K. W., ... Zhang, H. (2022). Attribution of space-time variability in global-ocean dissolved inorganic carbon. *Global Biogeochemical Cycles*, *36*(3), e2021GB007162.

de Boyer Montégut, C., Madec, G., Fischer, A. S., Lazar, A., & Iudicone, D. (2004). Mixed layer depth over the global ocean: An examination of profile data and a profile-based climatology. *Journal of Geophysical Research: Oceans*, *109*(C12). Retrieved from `https://onlinelibrary.wiley.com/doi/abs/10.1029/2004JC002378` doi: 10.1029/2004JC002378

Gregor, L., & Gruber, N. (2021). OceanSODA-ETHZ: a global gridded data set of the surface ocean carbonate system for seasonal to decadal studies of ocean acidification. *Earth System Science Data*, *13*(2), 777–808.

Humphreys, M. P., Lewis, E. R., Sharp, J. D., & Pierrot, D. (2022). PyCO2SYS v1.8: marine carbonate system calculations in Python. *Geoscientific Model Development*, *15*(1), 15–43.

Kara, A. B., Rochford, P. A., & Hurlburt, H. E. (2003). Mixed layer depth variability over the global ocean. *Journal of Geophysical Research: Oceans*, *108*(C3). doi: 10.1029/2000JC000736

Lauvset, S. K., Lange, N., Tanhua, T., Bittig, H. C., Olsen, A., Kozyr, A., ... Key, R. M. (2021). An updated version of the global interior ocean biogeochemical data product, glodapv2.2021. *Earth System Science Data Discussions*, *2021*, 1–32.

Olsen, A., Lange, N., Key, R. M., Tanhua, T., Bittig, H. C., Kozyr, A., ... Woosley,

R. J. (2020). An updated version of the global interior ocean biogeochemical data product, glodapv2.2020. *Earth System Science Data*, *12*(4), 3653–3678.

Reynolds, R. W., Rayner, N. A., Smith, T. M., Stokes, D. C., & Wang, W. (2002). An Improved In Situ and Satellite SST Analysis for Climate. *Journal of Climate*, *15*(13), 1609–1625.

Suga, T., & Hanawa, K. (1990). The mixed-layer climatology in the northwestern part of the North Pacific subtropical gyre and the formation area of Subtropical Mode Water. *J Mar Res*, *48*(3), 543–566. doi: 10.1357/002224090784984669

Zhou, M., Tyka, M. D., Ho, D. T., Yankovsky, E., Bachman, S., Nicholas, T., . . . Long, M. C. (2025). Mapping the global variation in the efficiency of ocean alkalinity enhancement for carbon dioxide removal. *Nature Climate Change*, *15*(1), 59–65.

Notes

1. `https://carbonplan.org/research/oae-efficiency`

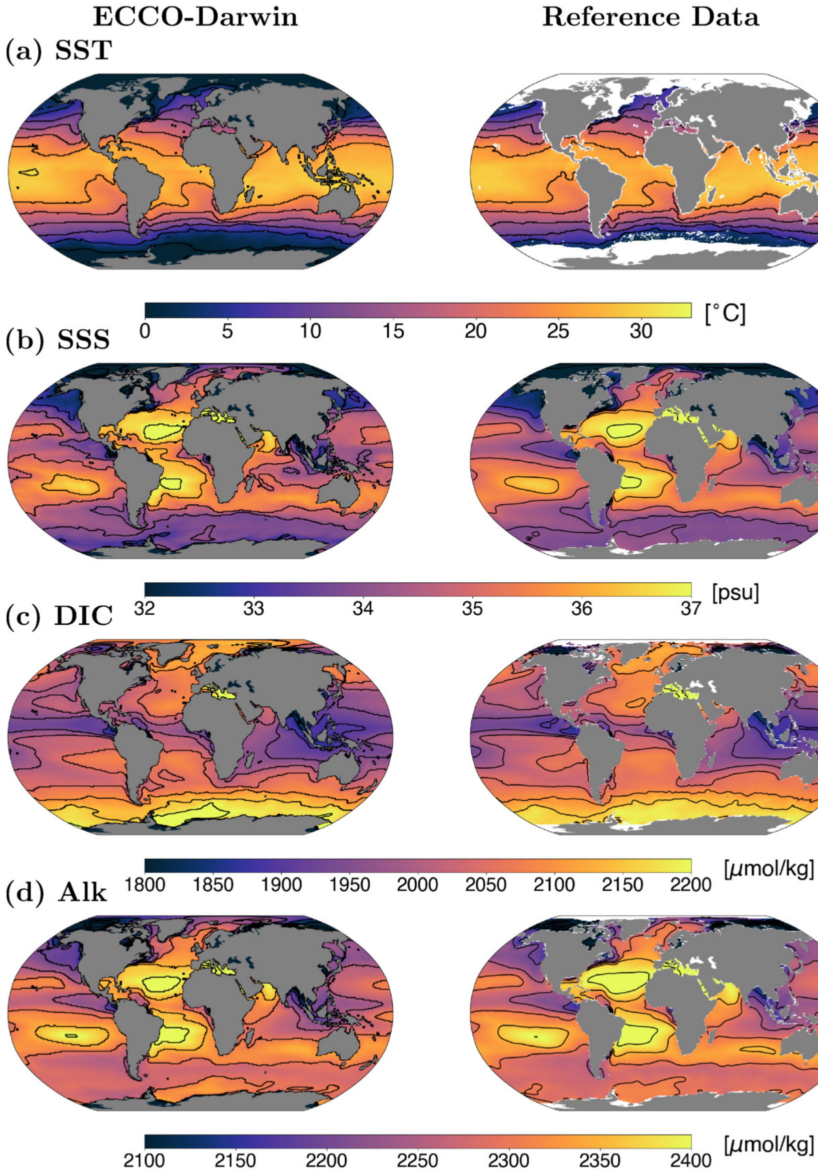

Figure S1. Comparison of time-mean (from January 1995 to December 2017) surface-ocean fields from the baseline ECCO-Darwin simulation against reference (a) sea-surface temperature (SST), (b) sea-surface salinity (SSS), (c) *DIC*, and (d) *Alk* . Reference SST is from Reynolds et al. (2002); all other reference fields are from OceanSODA-ETHZ (Gregor & Gruber, 2021).

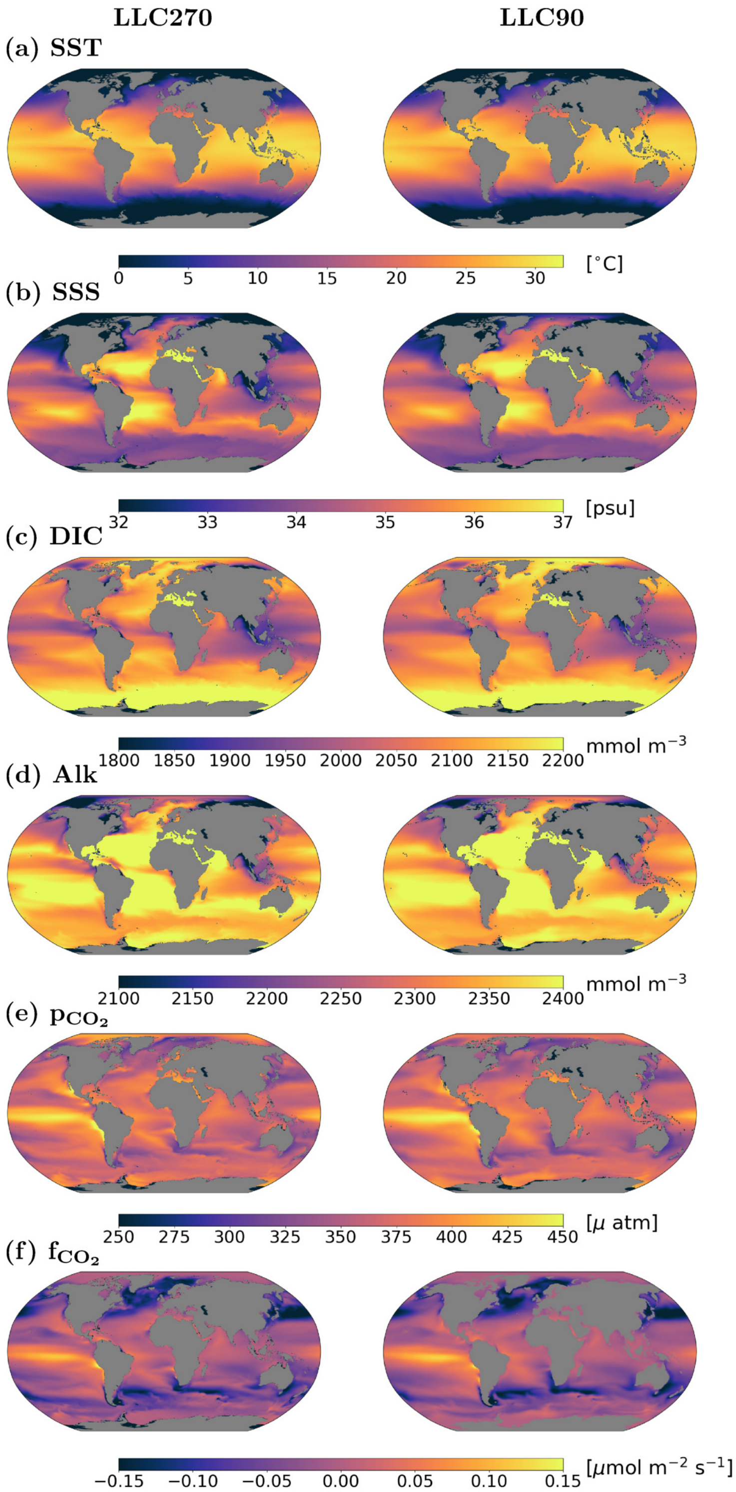

Figure S2. Comparison of time-mean (1995–2017) surface-ocean fields from ECCO-Darwin LLC 270 (Carroll et al., 2020) and the baseline ECCO-Darwin (LLC90 solution) used in this paper.

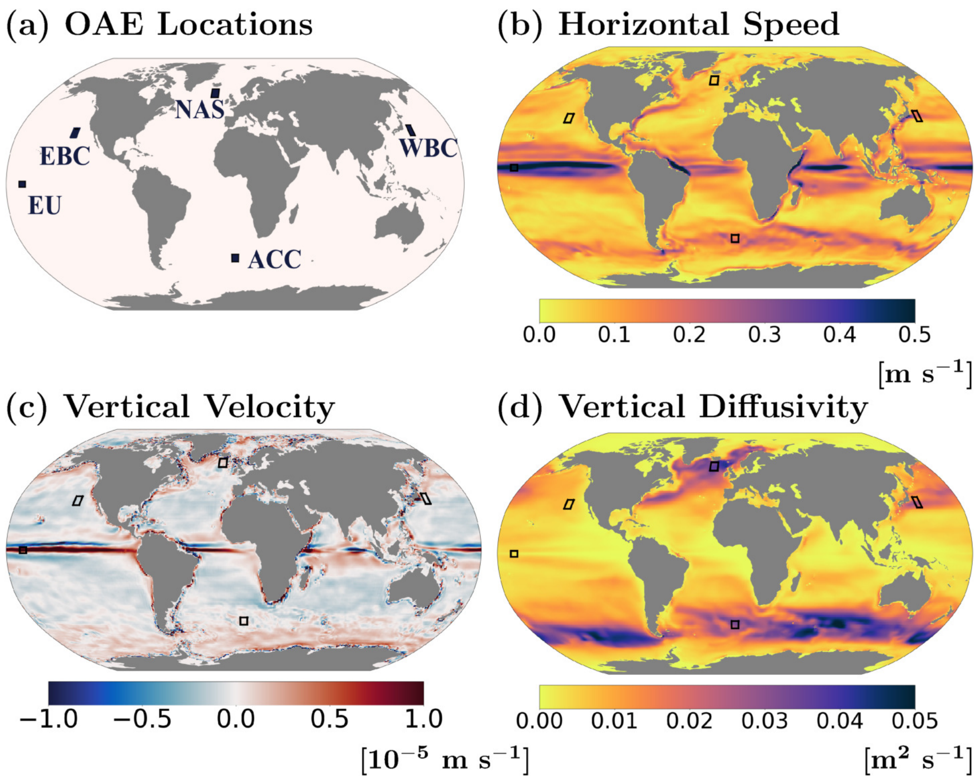

Figure S3. (a) OAE deployment sites and time-mean values (from January 1995 to December 2017) of (b) magnitude of surface-ocean horizontal velocity, (c) average vertical velocity in the upper 100 m, and (d) average vertical diffusivity in the upper 100 m.

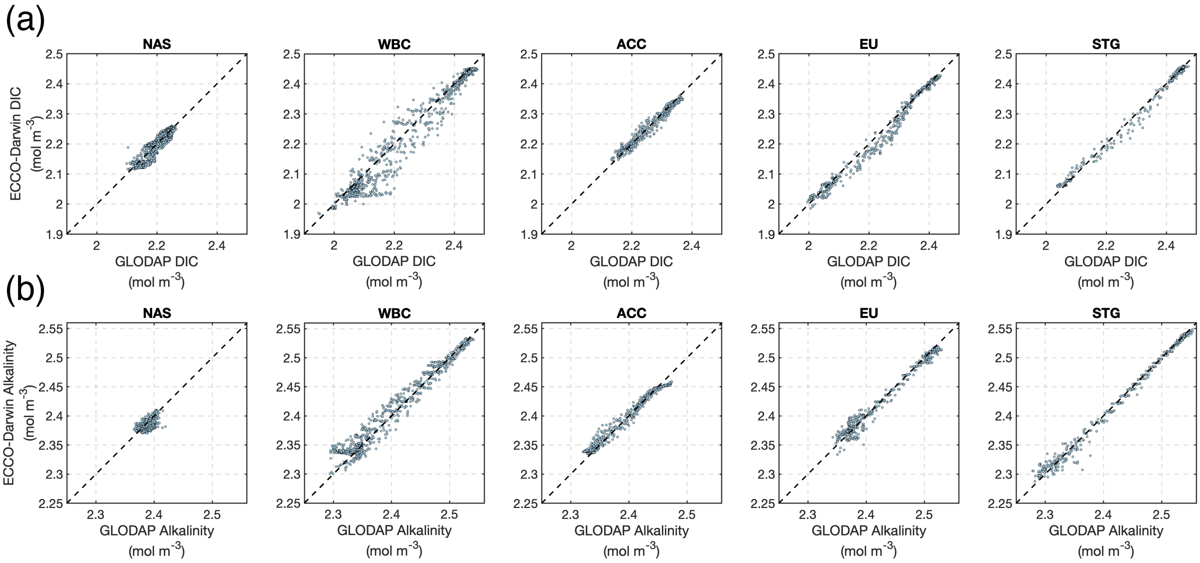

Figure S4. Comparison of the baseline ECCO-Darwin DIC and Alk against all GLODAPv2.2022 observations (Lauvset et al., 2021) at the 5 deployment sites. The x-axis shows observations and y-axis shows the corresponding monthly averaged model value taken at the closest space-time location.

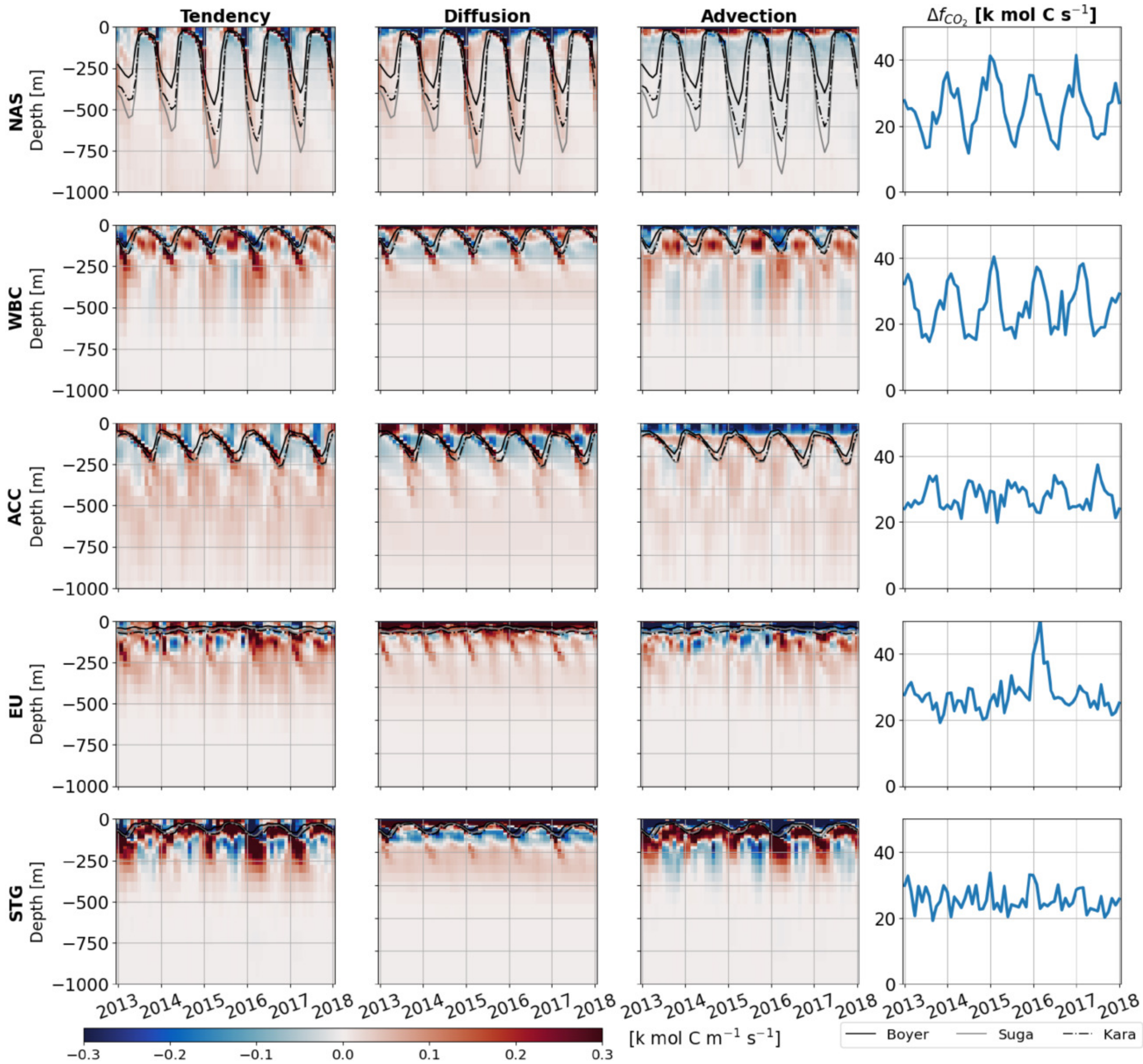

Figure S5. Horizontally-integrated budget terms from $\Delta\widehat{DIC}$ (Equation 4) for the 5 continuous OAE experiments over the last 5 years of simulation. Budget terms include: tendency, diffusion, advection, and air-sea CO_2 flux. Biological source terms are negligible and not shown. Three different mixed layer depth (black lines) are computed using Boyer, Suga, and Kara diagnostics and we plot the spatially averaged values over the OAE deployment sites.

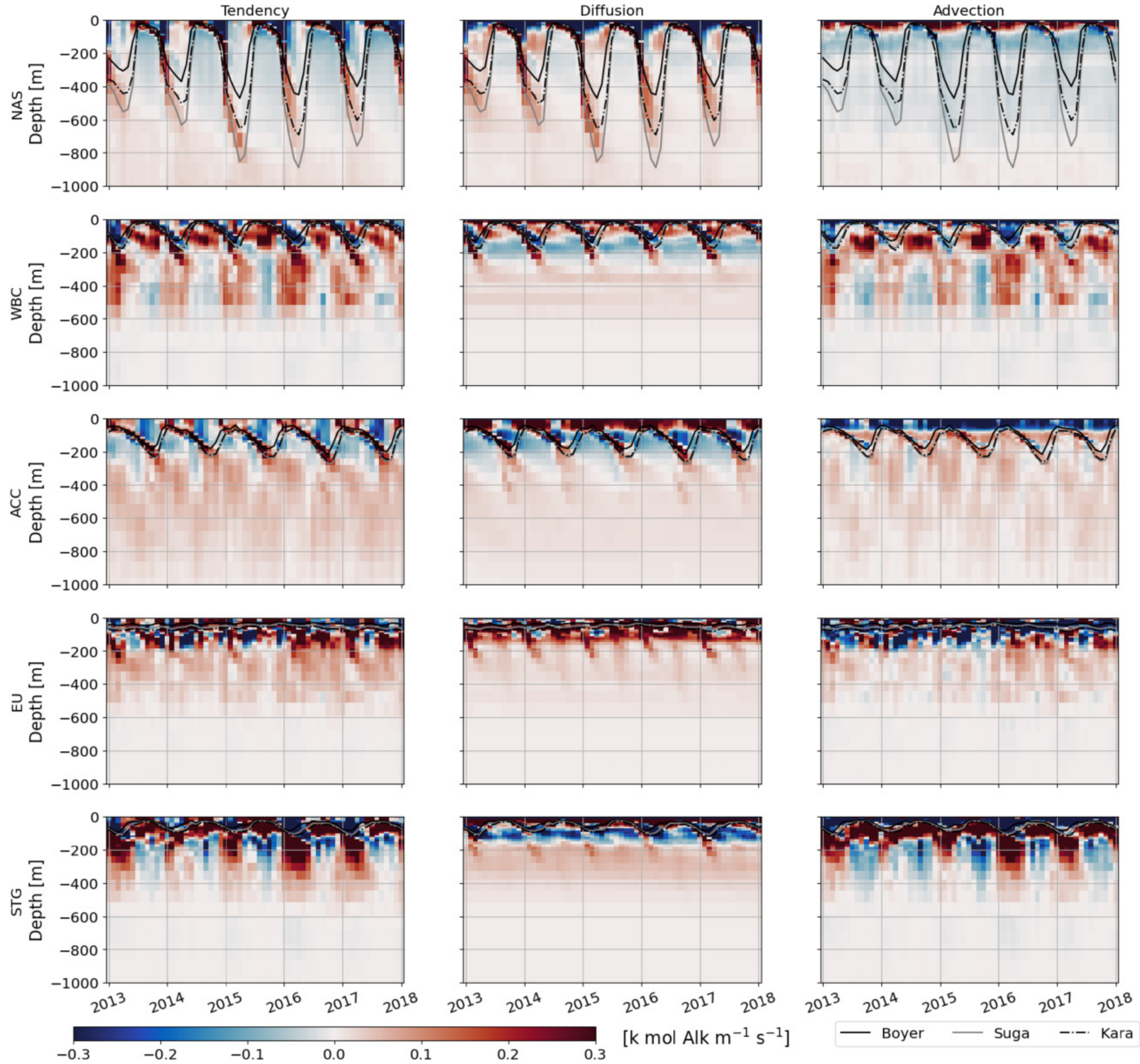

Figure S6. Horizontally-integrated budget terms for $\Delta\widehat{Alk}$ (Equation 5) for the 5 continuous OAE experiments over the last 5 years of simulation. Budget terms include: tendency, diffusion, and advection. Biological source terms are not shown because they are negligible; prescribed surface-ocean Alk flux is constant and is also not shown. Three different mixed layer depth (black lines) are computed using Boyer, Suga, and Kara diagnostics and we plot the spatially averaged values over the OAE deployment sites.

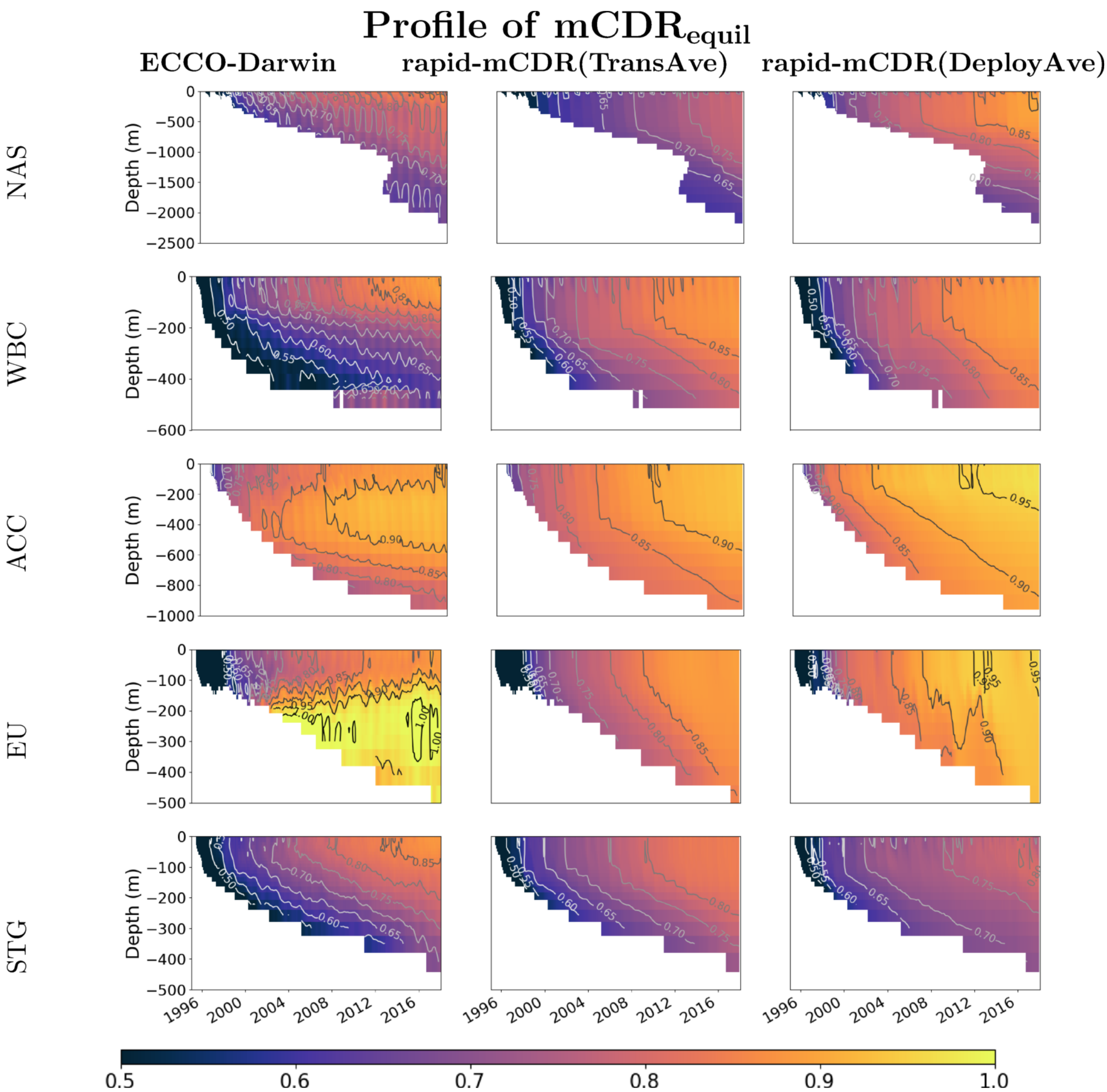

Figure S7. Comparison of time series of horizontally averaged, vertically-resolved $mCDR_{equil}$ from ECCO-Darwin (left panel) and both versions of rapid-mCDR (middle and right panels).

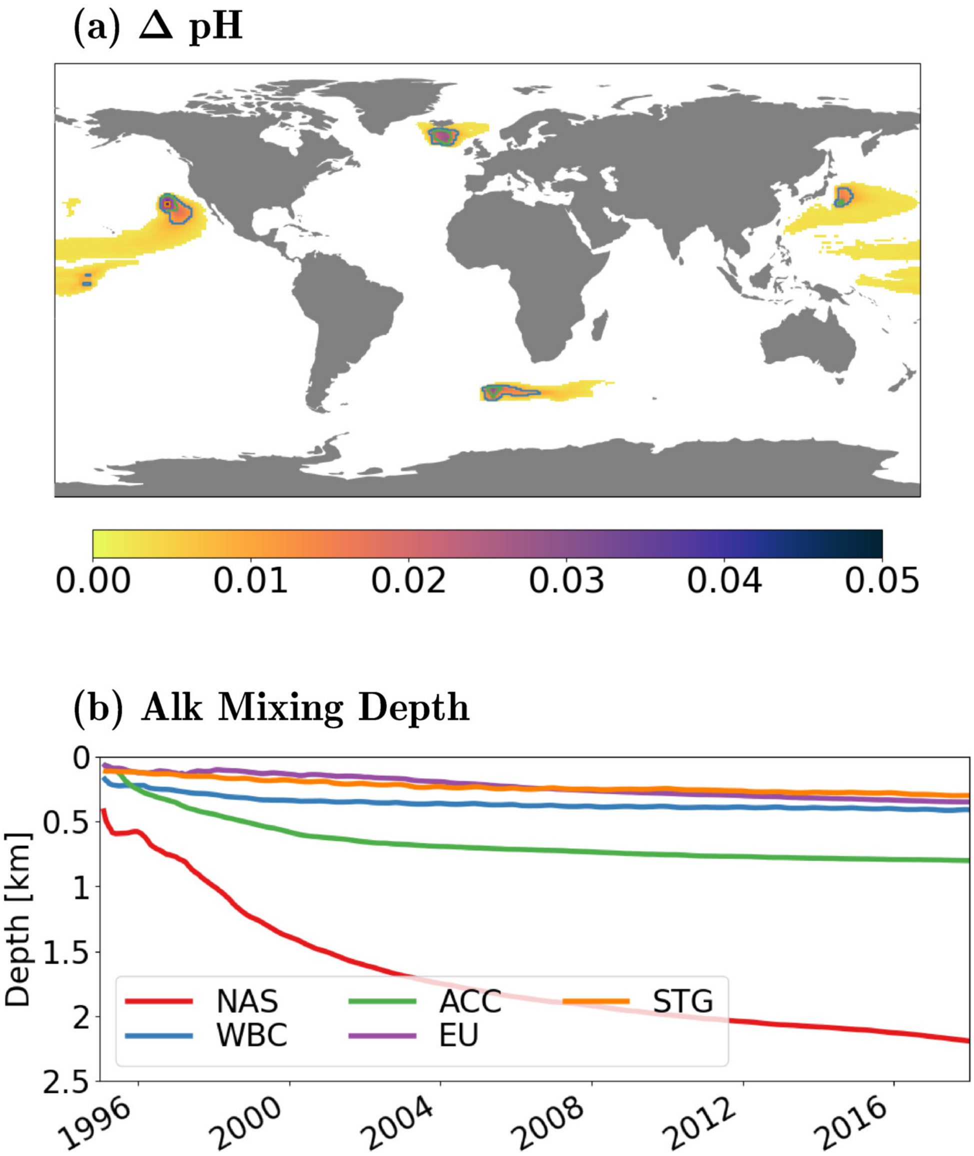

Figure S8. Continious OAE experiments: (a) Maximum pH perturbation across time and depth (maximum Δ pH) due to OAE for the 5 continuous experiments. Only values above 0.0025 are shown. Isolines represent maximum ΔpH values of 0.01, 0.02, 0.03, and 0.04. (b) Time series of the depth that separates OAE-impacted waters from unmodified waters. This depth is such that 95% of ejected alkalinity stays above it.

ED deployments	Polygons from Zhou et al. (2025)
NAS	32, 52, 128, 138
ACC	509, 530, 629, 635

Table S1. Polygon indices from Zhou et al. (2025) on CarbonPlan website used for comparison with ECCO-Darwin deployments.

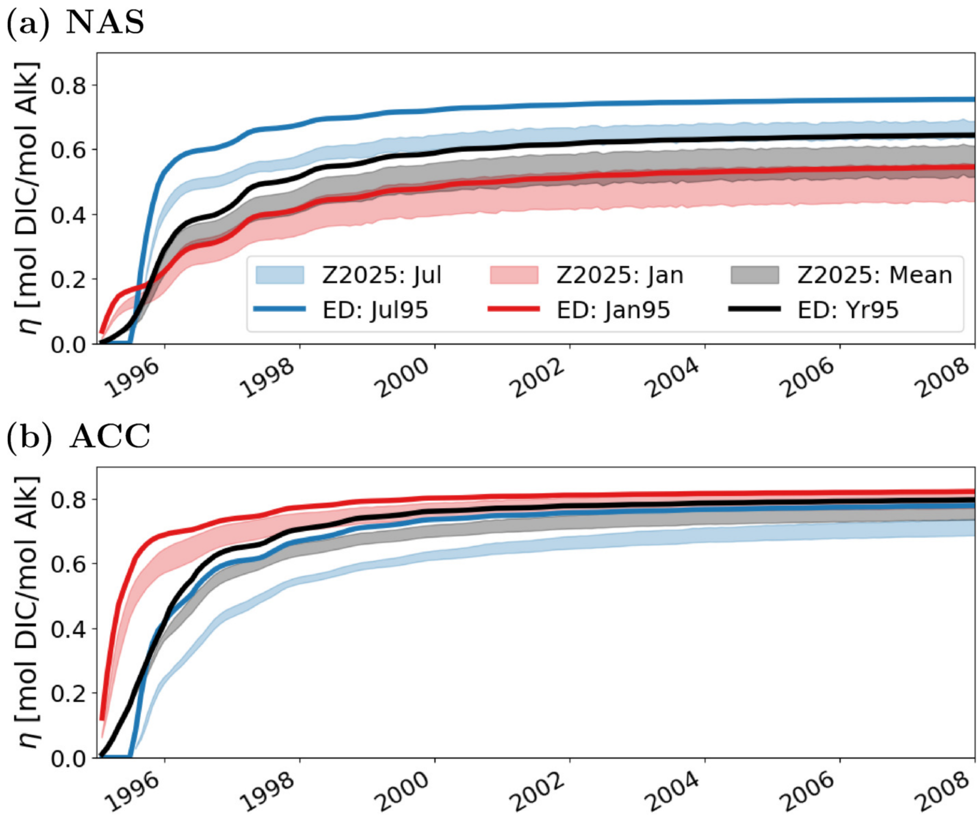

Figure S9. Net CO_2 Uptake Efficiency (η) from ECCO-Darwin: monthly pulse Deployments (July 1995 – Blue; January 1995 – Red), Yearly 1995 Deployment (Black), and Zhou et al. (2025) Ranges (Shaded Areas). The Zhou et al. (2025) ranges are derived from the spread of simulations from the four nearest polygons to our deployment sites (polygon indices are shown in Table S1). The yearly ECCO-Darwin deployment is compared to the mean efficiency of four monthly deployments from Zhou et al. (2025). Note that the experiments of Zhou et al. (2025) were initialized in the year 1999, but the initial year is shifted to 1995 on the plot for comparison. Panel (a) for NAS and (b) for ACC deployment locations.